POLITECNICO DI TORINO

Corso di Laurea Magistrale

in Ingegneria Meccanica

Tesi di Laurea Magistrale

CFD-FEM analysis of the vessel-FLiBe tank interaction of an ARC-like fusion reactor in disruption events

Relatori
Prof. Massimo Zucchetti
Dr. Raffaella Testoni

Corelatori
Stefano Segantin

Candidato
Nicola Alberto Cimmino

Anno Accademico 2020/2021

Sommario

Grazie all’avvento di nuove tipologie di magneti superconduttori ad alta temperatura di esercizio è stato possibile realizzare reattori a fusione nucleare, o *tokamaks*, il cui design costruttivo permette una facile installazione e rimozione dei magneti stessi che lo compongono. Tale innovazione tecnologica permette di facilitare la costruzione di reattori di nuova generazione caratterizzati da configurazioni sempre più modulari e semplificate. All’interno di questo quadro tecnologico, il Massachusetts Institute of Technology è al lavoro per realizzare una nuova tipologia di reattore a fusione: il reattore ARC (Affordable Robust Compact), il cui design può essere schematizzato mediante un sottile guscio interno in lega metallica, definito vacuum vessel, all’interno del quale avvengono reazioni di fusione DT che generano plasma a temperature di oltre cento milioni di kelvin. Questo è inoltre sottoposto a un regime di vuoto spinto e circondato interamente da un sale fuso ad alta temperatura, chiamato FLiBe, posto all’interno di una vasca.

Dal punto di vista della sicurezza del reattore è necessario analizzare accuratamente l’interazione tra il guscio interno in lega e il sale fuso nella vasca, con particolare attenzione al caso in cui incidenti più o meno gravi modifichino l’equilibrio tra i due elementi. Uno degli incidenti più caratteristici per un reattore a fusione è la “plasma disruption”, evento che può compromettere in modo irreparabile il funzionamento del reattore stesso. Mentre vari studi si sono riproposti di analizzare il problema della simulazione di una disruption dal punto di vista elettromeccanico, concentrandosi quindi sull’interazione plasma-guscio, il presente studio vuole proporre una strategia di modellazione concentrata sull’interazione guscio-sale fuso nel caso immediatamente successivo alla disruption.

Lo studio mostra che il vessel, in base ai vincoli progettuali proposti in fase di modellazione, si comporta in modo analogo ad un pendolo smorzato. Le forze viscose del sale fuso, quindi, agiscono come smorzatore nei confronti del vessel, mentre il campo di pressioni all’interno del serbatoio genera onde caratterizzate da una ampiezza decrescente in funzione del tempo, perlomeno fino al possibile insorgere di fenomeni di turbolenza.

Per quanto riguarda quindi l’interazione fluido-struttura, lo studio propone una strategia di modellazione basata su un’analisi dinamica mediante tecniche FEM-CFD.

Abstract

The advent of high temperature superconductors enables the feasibility of the technology of tokamaks with demountable magnets. Such technological breakthrough opens for new and simplified reactor core configurations. In this framework, Massachusetts Institute of Technology is working to design a new fusion reactor generation: Affordable Robust Compact (ARC) reactor. ARC design is characterized by a bulk liquid blanket tank of FLiBe molten salt which fully surrounds the thin vacuum vessel where DT reactions take place that generate fusion plasma over a hundred million kelvin.

From a safety point of view the vessel-blanket interaction must be carefully analysed, especially in case of accidents. One of the most characteristic accidents of a fusion machine is the plasma disruption, event that could heavily damage the reactor core components. While several studies tackled the problem of simulating disruptions through electromechanical models, paying a special attention on the plasma-vessel interaction analysis, the current thesis proposes a modelling strategy for the vessel interaction with the fluid blanket immediately after the disruption had occurred. The study shows that the vessel, under the proposed constraints, acts like a damped pendulum where the viscous forces of the FLiBe acts as a damper. At the same time, inside the tank pressure forces creates fluid waves of decreasing amplitude as a function of time, up to the possible unset of turbulence phenomena. Therefore, regarding the structure-blanket interaction, this work proposes a time evolution FEM-CFD modelling strategy.

Contents

Chapter 1

1 Introduction

The presented thesis is a result of the collaboration between the Energy department of Politecnico di Torino (DENERG) and the Plasma Science and Fusion Center (PSFC) of the Massachussets Institute of Technology. Its main goal is to show qualitatively that the vessel, under the proposed constraints, acts like a damped pendulum where the viscous forces of the FLiBe acts as a shock absorber, creating pressure waves inside the tank of decreasing amplitude as a function of time.

1.1 Reactor scheme

The ARC (Affordable Robust Compact) reactor is an innovative design of pulsate tokamak with demountable magnets capable of reaching power of 525 MW in a compact solution. It presents itself with an internal toroidal chamber, defined as Vacuum Vessel, where the fusion reaction is achieved by means of insertion of Deuterium and Tritium as a fuel (Fig. 1).

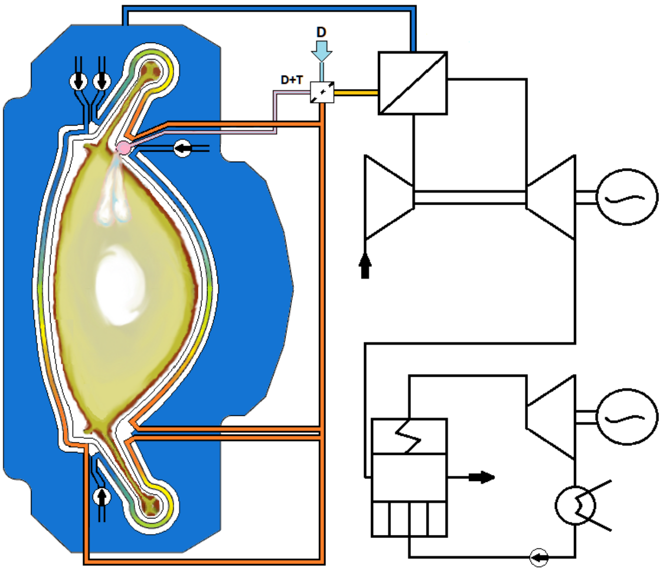

Fig. 1 - General layout of an ARC energy production power plant plant

Deuterium and Tritium are both isotopes of Hydrogen, but while the former has no radioactivity the latter is presented as a beta-emitting isotope of the element, classified as a highly dangerous radioactive element due to its considerable volatility. While it is necessary to produce the deuterium outside the reactor, unlike all the other solutions the ARC reactor satisfies its Tritium needs internally through the process of the Tritium breeding inside the cooling system.

The D +T blend should be pumped inside the vessel with Hydrogen pumps, and ignited via some kind of ITER like ion cyclotron heating system [1] to achieve the following reactions.

$$D + T = {}^{4}He + n + 17.6\ MeV \tag{1.1}$$

$$T + T = {}^{4}He + 2n + 11.3\ MeV \tag{1.2}$$

$$T + T = {}^{3}He + n + 3.2\ MeV \tag{1.3}$$

$$D + D = T + p + 4\ MeV \tag{1.4}$$

$$D + {}^{3}He = {}^{4}He + p + 18.3\ MeV \tag{1.5}$$

D+T reactions (1.1-4) are likely to happen at relatively low temperatures (around 175 millions kelvin) while the D-He3 reaction (1.5) needs a very high ones (above 540 millions kelvin). For this reason the first reaction is the one we are interested in due to its high probability to happen and because it’s the most energetic one among those presented above. This generates plasma that needs to be as pure as possible and must be retained inside the vessel; to do so the demountable HTS (High Temperature Superconductors) magnets produce a magnetic field of 9T in a environment at relatively high temperatures compared to canonical superconductors ones [2].The magnetic confinement of plasma is probably one of the most peculiar aspect of this type of machines, and is achieved by a sets of magnets: the central solenoid wich modulate the plasma current and also act as a confinement device; the poloidal field coils that acts as a confinement device and drags impurities out of plasma directing them towards the divertors. A high amount of Radiation and Neutron heat is thus generated and must be drawn by the cooling system, represented by the turbulent liquid FLiBe layer inside the vessel.

All the components are then immersed in the melted salt inside the FLiBe Tank, where around 700 tons of fluid prevents the escape of neutrons overtime from the main energy production system. This liquid blanket, a great innovation with respect to other tokamak concepts, would also act both as a fluid capacity in the first energy gathering cycle and as a fluid dumper for the vessel in case of some types of disruptions.

1.2 Vacuum Vessel

The Vacuum vessel, which can also be reduced to the acronym VV, is so called beacuse of its high vacuum properties and is conceived as a multi-layer toroidal vessel capable of holding the plasma where the fusion reaction is achieved. Because of such high temperatures the heat cannot be extracted directly by conduction or convection, the extreme vacuum therefore guaranteing that heat propagates to the layers by radiations or neutron flux. Only later by neutron energy deposition, by convective and conductive mechanisms the heat is exchanged between solid and fluid layers. The ARC vessel concept, contrary to ITER’s radial slices, is conceived as a single piece allowing an easy axial disassembly of the reactor, and equipped with all the necessary sensors and outer side ports that allow maintenance by technicians. The structure is then clearly subject to thermal fatigue phenomena but, owing to the neutron flux, is subject also to mechanical and thermal properties degradation wich leads to remarkable considerations in the sizing of the various layers.

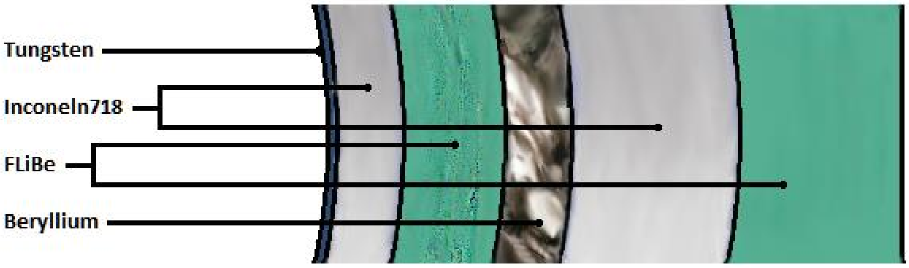

Fig. 2 - Vacuum Vessel layers layout

Going on moving towards the innermost layer of the vessel we find the so called “first wall” (Fig.2), a small shell which is contrieved to be capable of different tasks: to have an high melting point in order to withstand surface temperatures; to have an high thermal conductivity in order to mitigate the temperature gradients across its section; to match thermal expansion phenomena of other layers in order to avoid tensions between them; and,last but not least, to avoid tritium retention. For the reasons above mentioned, the optimal up-to-date choice lies in the use of a 1mm tungsten layer that has both low high-temperature corrosion and tritium retention properties.

The structural material of the vessel is furthermore represented by two layers of Inconel 718, a high-strength corrosion-resistant nickel chromium alloy. That material shows a low magnetic permeability reducing both interactions between vessel and magnetic field and distortions of magnetic lines. These layers, in order to carry out their function, have been found to be viable with a thickness of, respectively, 10mm the innermost and 30mm the outermost, whereas a change in thickness is currently being evaluated due to the reduction of thermal effects and in order to allow possible downsizing of the structure leading to a reduction of costs, weigh and radioactive waste. As regards thermal expansion, this is in fact caused by both thermal gradients across the section and gradients across the vessel profile. Therefore, considering a low tollerance in vessel dimensions variation along the profile, all to ensure proper operation of the reactor, the phenomenon must be carefully taken into account both from a stationary and a dinamic fatigue point of view. As a structural point of view, on the other hand, the chamber is subject to both the forces deriving from the structure's own weight and to the buoyancy forces due to its immersion inside the FLiBe tank.

Between the two metal layers there is a layer of FLiBe molten salt which acts as cooling system and tritium conveyor (which will be discussed later), and a layer of beryllium which works both as a neutron multiplier and as a tritium breeder.

Even using the inconel alloy, or Vanadium alloy as it is studied nowadays, the structure is subject to conspicous embrittlement over a short period of time. For this reason, the vessel will be substituted after about two full power years.

1.3 Divertors

All of the heat power produced by the fusion reaction has to be managed in some way. More than a half of it, as mentioned in the ARC reactor scheme, should be exhausted in the form of radiative and neutron fluxes by the FLiBe circuit; but a great part of heat, added with impurities from the tungsten wall, is directed through the outer plasma scrape-off layer to the divertors. These substantially work as heat exhaust and as plasma cleaner, their geometry and sub-components are actively investigated in the ARC concept to provide a mean to tackle the two challenges.

1.4 Flibe Loop

The FLiBe is a salt with a melting point around 733K, a high volumetric heat capacity and a low vapour pressure at high temperatures. Thanks to these properties, it is usefull as a coolant and it could also work well in the heat storage environment. As stated above the blanket and the vessel layer work as a tritium breeder by means of the basic nuclear processes [3];

$$^{6}Li + n = \ ^{4}He + T + 4.78MeV \tag{1.6}$$

$$^{7}Li + n = \ ^{4}He + T + n - 2.47MeV \tag{1.7}$$

The first one, due to its exothermic nature and its considerable probability to generate Tritium , is the most interesting and at the same time the most difficult to achieve because of the scarce presence of ^{6}Li as a lithium isotope (7.5%). ^{7}Li, on the contrary, is the most abudant isotope in nature (around 92.5%) and that means that, in order to take advantage of the first process, the lithium must be enriched to ^{6}Li. [4]

As a matter of fact the tritium has been lately produced in reactors operating specifically for tritium and plutonium production, bombarding the non-radioactive lithium with neutrons [5]. Concerns regard, of course, the safely handling of the radioactive material from the production source to the usage fusion reactor, which presupposes a huge financing from a transport safety and tritium storage point of view.

Reactors based on the DT reaction, on the contrary, are capable of producing its own needs of tritium thanks to the safety of two layers with high neutron absorption capacity.

The tritium cycle sustainability is thus evaluated through the use of the TBR (tritium breeding ratio) coefficient:

$$TBR = \frac{Amount\ of\ {}^{3}H\ generated\ in\ blanket}{Amount\ of\ {}^{3}H\ burnt\ in\ plasma} \tag{1.8}$$

Which has to be larger than 1 to sustain the whole reaction cycle. In order to do so the beryllium VV layer acts as a neutron multiplier, based on the reaction:

$$^{9}Be + n = \ 2^{4}He + 2n \tag{1.9}$$

Providing so enough neutrons for the TBR to be greater than 1.

Before entering the heat exchanger, in order not to influence them with corrosive and embrittlment phenomena, the tritium is removed from the FLiBe by means of permeative filters that work continously.

The FLiBe melting point, however, sets the safe lower temperature of the first energy transfer cycle which is 800 K. Therefore, all the fluid collected from the blanket, and the whole blanket itself, can be considered as a thermic capacity and evenly set to this lower temperature. From previous studies on VV thermal behaviour it emerges that a good estimation on the escape temperature of the liquid salt from the vessel is around 870 K, which sets the highest temperature of the first cycle and consequently the working values for the heat exchanger. The outlet temperature of the system may appear extremely low compared to the ones involved in the fusion reaction. However, it should not be forgotten that the temperature gradient between plasma and first wall is particularly high, the latter reaching temperatures in order of thousand degrees. Fact that imply a great variety of thermal gradients along the structure, but an under-sizing of the vessel is being assessed in order to achieve the desired tolerances once the reactor operates at full load.

1.5 Magnetic confinement

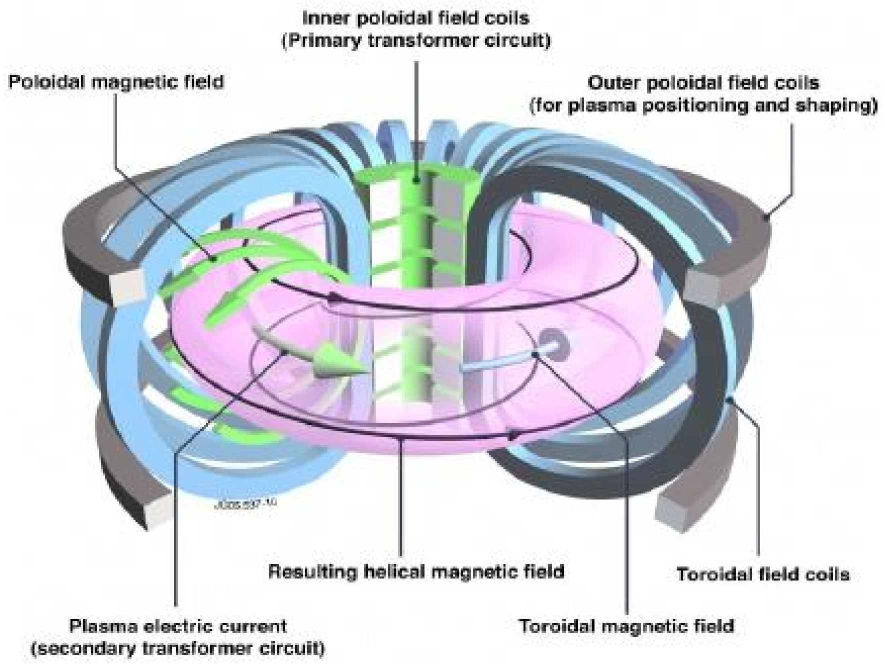

Fig. 3 - Toroidal and Poloidal field coils rappresentation

As a matter of fact, the human being do not yet know materials capable of being placed in contact with plasma without liquefying or sublimating. This being the situation, the solution found proposes an infinite magnetic loop that holds the plasma far away enough from the VV. In order to achieve the necessary magnetic field shape, different kind of coils are used to obtain the loop (Fig.3): a set of toroidal field coils and two set of poloidal field ones (Inner and Outer). In ARC, the long legged divertors are also provided with specific coils to sustain their functionality adding complexity in the definition of forces and stresses involved on the vessel structure.

The chamber is hence subjected to shear stresses caused by the twisting moments exerted by the magnetic field-structure interaction, but at the same time mitigated from the low magnetic permeability of the materials. At any rate, more studies must be conducted on the subject to define the extent of these stresses.

To allow the intensity of the magnetic field necessary to contain the plasma, the magnets are set at 30 K, an extremely high working temperature compared with the previously hypothized for the LTS of less than 4 K.

Chapter 2

2 Mathematical definition of the model

As previously stated, aim of the thesis is that of providing a modelling technique that correctly represents the mutual interaction of the vessel with the surrounding FLiBe blanket in consequence of a disruption event to the reactor. Clearly, defining closed-form equations for the mathematical solution of such a complex problem is not a simple task. From a mechanical point of view thin layer theories do not provide enough informations on the stress behaviour of the structure and is therefore requested an analysis along the thickness of the vessel itself. Solutions have been found in the papers previously presented, such as the stress function method, to determine stress and displacements configuration under variable loads on simple geometrical thick objects (spheres, cylinders). None of them, though, were developed for a highly variable geometry structure nor for a multilayer one. From a fluid dinamic point of view defining analytical dynamic equations deriving from the NS system is far too complicate for elaborate shapes geometry and this is exactly the reason that justifies the use of a CFD module.

Because of the above mentioned, in the current analysis the problem of a thick cylinder of Inconeln718 immersed in a fluid, under the proposed boundary conditions, was analyzed by means of the Lamè equations, the Archiemde's Law and the COMSOL fluid-structure interaction modelling tool. The goal was to provide a two-dimensional, simplified model for the vessel-blanket couple that could be statically validated using closed form equations for both the stress of the structure and the force exerted by the fluid blanket on it, defined as Lift. Lift, along with Drag force, will then be used in chapter 3 to show the dynamic behaviour of the couple in the three-dimensional upgraded model. The general equations used to define the mathematical model as well as the equations used by COMSOL in order to obtain the results are presented below.

2.1 Disruptions

As explained in the first section the fusion reaction generates neutrons and ^{4}He ions; while the former escape the magnetic field reaching VV and blanket the latter need to sustain the fusion conditions giving off their energy to mantain the heat power.

He ions, also called "alpha particles", can resonate with magnetohydrodinamic (MHD) waves generated inside the plasma itself leading to inhomogeneities and instabilities that can grow in amplitude with a deleterious impact on heat transfer, creating potential problems to the structural integrity of the tokamak.

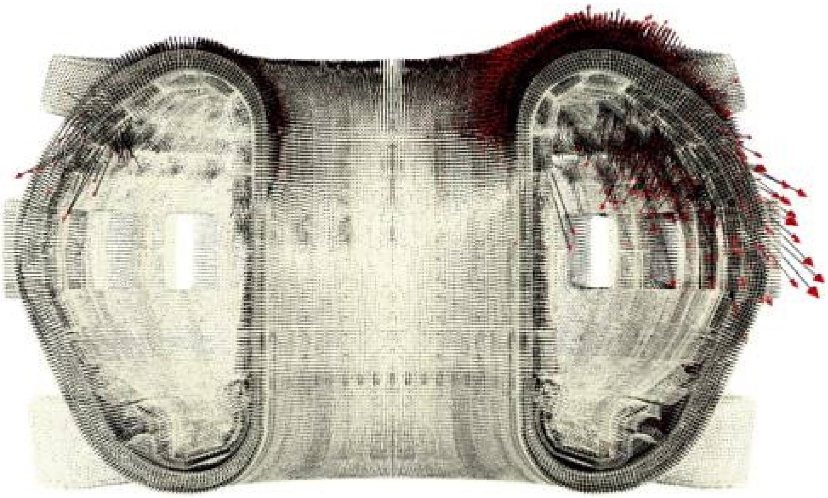

Fig. 4 - Force distribution on ITER during a symmetrical VDE

Instability events let, as a matter of fact, the plasma core stay on and are not disruptive for the vessel integrity, but there are different kind of events from wich the reactor cannot recover, driving to a terminal failure of reactor operativity: disruptions. These can occur for various reasons such as great instabilities or "first wall" fragments trapped inside the plasma, but can also be caused by (or even cause) a Vertical Displacement Event (VDE) of the plasma column. Plasma control loss is a serious issue: firstly for the vessel wall where the high thermal gradient can cause melting, this is the "thermal quench" which tipically occurs in less than milliseconds; secondly for several MA of plasma current flowing through the vessel layers, also defined as "current quench". These currents, assumed the high magnetic field that exists in the VV, cause halo currents imposing huge forces on the structure which have yet to be extensively defined both in magnitude and distribution.

There are papers that analyze the effects on ITER of a symmetrical VDE from a hydromagnetic point of view, taking into account only forces produced by the interaction of halo currents and the toroidal magnetic field. Results show that force distribution is widely varied and can be even more particular in case of an asymmetric vertical displacement event (AVDE). [6]

Avoiding then a pre-analysis with an MHD model, the reductive hypotesis of a punctual impulse force has been adopted in this document, clearly not including in the analysis possible torque moments along the toroidal plane. These, in any case, would not bring about any significant modification of the fluid dynamic behaviour. Therefore, a Gaussian pulse condition was used on the COMSOL model trying to define a magnitude validity range as well as present possible forces configuration.

2.2 Mechanical formulation

The stress tensor σ_{ij} caused by forces exerted is below represented, both as a linear equation and as a matrix form, in the form of a linear combination of the hydrostatic stress tensor p and the deviatoric stress tensor s_{ij}. It can be presented using Einstein notation

$$\sigma_{ij} = s_{ij} + p\delta_{ij}\, where\; p = \frac{1}{3}\sigma_{ii} = \frac{1}{3}(\sigma_{xx} + \sigma_{yy} + \sigma_{zz}) \tag{2.1}$$

$$\sigma_{ij} = \begin{bmatrix} s_{xx} - p & \sigma_{xy} & \sigma_{xz} \\ & s_{yy} - p & \sigma_{yz} \\ symm & & s_{zz} - p \end{bmatrix} \tag{2.2}$$

Deformations can as well be represented in a matrix form

$$\underline{\underline{\varepsilon}} = \begin{bmatrix} \varepsilon_{xx} & \varepsilon_{xy} & \varepsilon_{xz} \\ & \varepsilon_{yy} & \varepsilon_{yz} \\ symm & & \varepsilon_{zz} \end{bmatrix} \tag{2.3}$$

And for an isotropic material ($E_x = E_y = E_z$) with $G = \frac{E}{2(1+\nu)}$

$$\begin{bmatrix} \varepsilon_{xx} \\ \varepsilon_{yy} \\ \varepsilon_{zz} \\ 2\varepsilon_{xy} \\ 2\varepsilon_{xz} \\ 2\varepsilon_{yz} \end{bmatrix} = \frac{1}{E} \begin{bmatrix} 1 & -\nu & -\nu & 0 & 0 & 0 \\ & 1 & -\nu & 0 & 0 & 0 \\ & & 1 & 0 & 0 & 0 \\ & & & 2(1+\nu) & 0 & 0 \\ & symm & & & 2(1+\nu) & 0 \\ & & & & & 2(1+\nu) \end{bmatrix} \cdot \begin{vmatrix} \sigma_{xx} \\ \sigma_{yy} \\ \sigma_{zz} \\ \sigma_{xy} \\ \sigma_{xz} \\ \sigma_{yz} \end{vmatrix} \tag{2.4}$$

Principal stress components can then be combined to form stress invariants

$$I_1 = tr\left(\underline{\underline{\sigma}}\right) = \sigma_{xx} + \sigma_{yy} + \sigma_{zz} \tag{2.5}$$

$$I_2 = \frac{1}{2}\left[\left(tr\left(\underline{\underline{\sigma}}\right)\right)^2 - tr\left(\underline{\underline{\sigma^2}}\right)\right] = \sigma_{xx}\sigma_{yy} + \sigma_{xx}\sigma_{zz} + \sigma_{yy}\sigma_{zz} - \tau_{xy}^2 - \tau_{xz}^2 - \tau_{yz}^2 \tag{2.6}$$

$$I_3 = det\left(\underline{\underline{\sigma}}\right) \tag{2.7}$$

And the stress is so evaluated with Von Mises yield criterion

$$\sigma_{eq} = \sqrt{\sigma_{xx}^2 + \sigma_{yy}^2 + \sigma_{zz}^2 - \left(\sigma_x\sigma_y + \sigma_y\sigma_z + \sigma_z\sigma_y\right) + 3\left(\tau_{xy}^2 + \tau_{yz}^2 + \tau_{zx}^2\right)} \tag{2.8}$$

COMSOL actually calculates the σ_{eq} starting from the invariants of the stress deviator tensor $\underline{\underline{s}}$

$$\underline{\underline{s}} = \begin{bmatrix} \sigma_{11} - p & \sigma_{12} & \sigma_{13} \\ & \sigma_{22} - p & \sigma_{23} \\ symm & & \sigma_{33} - p \end{bmatrix} \tag{2.9}$$

$$I_1 = tr\left(\underline{\underline{s}}\right) = 0 \tag{2.10}$$

$$I_2 = \frac{1}{2}\left[\left(tr\left(\underline{\underline{s}}\right)\right)^2 - tr\left(\underline{\underline{s^2}}\right)\right] = -\tau_{xy}^2 - \tau_{xz}^2 - \tau_{yz}^2 \tag{2.11}$$

$$I_3 = det\left(\underline{\underline{s}}\right) \tag{2.12}$$

And the stress is consequently evaluated by the program with Von Mises criterion via the equation

$$\sigma_{eq} = \sqrt{3I_2} = \sqrt{3\left(\tau_{xy}^2 + \tau_{yz}^2 + \tau_{zx}^2\right)} \tag{2.13}$$

2.3 Fluid dynamic formulation

There is no doubt that every CFD model is based on the Navier Stokes Fourier system. The system is below expressed in punctual form, leaving out equations related to the total energy and to the heat transfer, as

$$\begin{cases} \dfrac{\partial\rho}{\partial t} + \nabla\cdot\left(\rho\underline{u}\right) = 0 \\ \dfrac{\partial\left(\rho\underline{u}\right)}{\partial t} + \nabla\cdot\left(\rho\underline{u}\times\underline{u}\right) + \nabla\cdot\left(p\underline{\underline{I}}\right) = \nabla\cdot\underline{\underline{\Pi_v}} + \rho\underline{g} \end{cases} \tag{2.14}$$

$$\underline{\underline{\Pi_v}} = \rho\nu\left(\nabla\underline{u} + \nabla\underline{u}^T - \frac{2}{3}\left(\nabla\cdot\underline{u}\right)\underline{\underline{I}}\right) \tag{2.15}$$

Considering a stationary point of view the dinamic viscosity is neglegible and the system can be further reduced to the Euler Equation

$$\begin{cases} \dfrac{\partial\rho}{\partial t} + \nabla\cdot\left(\rho\underline{u}\right) \\ \dfrac{\partial\left(\rho\underline{u}\right)}{\partial t} + \nabla\cdot\left(\rho\underline{u}\times\underline{u}\right) + \nabla\cdot\left(p\underline{\underline{I}}\right) = \rho\underline{g} \end{cases} \tag{2.16}$$

And it can be written in a lagrangian form as

$$\begin{cases} \dfrac{D\rho}{Dt} + \rho\nabla\cdot\underline{u} = 0 \\ \rho\dfrac{D\underline{u}}{Dt} = -\nabla\cdot\underline{\underline{\Pi}} + \rho\underline{g} \end{cases} \tag{2.17}$$

The strain tensor for a Newtonian liquid can then be represented by the linear combination [7]

$$\underline{\underline{\Pi}} = \underline{\underline{\Pi_s}} + \underline{\underline{\Pi_D}} \tag{2.18}$$

$$\tau_{ij} = -\left(p_m + \frac{2}{3}\mu\nabla\cdot\overline{v}\right)\delta_{ij} + \mu\left(\frac{\partial v_i}{\partial x_j} + \frac{\partial v_j}{\partial x_i}\right)\ where \begin{cases} i = j \ \rightarrow \delta_{ij} = 1 \\ i \neq j \ \rightarrow \delta_{ij} = 0 \end{cases} and\ p_m = -\frac{\tau_{ii}}{3} \tag{2.19}$$

Where p_m is the mechanical pressure and p represents the thermodynamic pressure.

On experimental grounds basis p_m is provided by the combination of two terms in the formula $p_m = p - \lambda\nabla\cdot\overline{v}$ where λ is the expansion viscosity. Only when density changes are induced either over extremely small distances or over very short time scales the term $\nabla\cdot\overline{v}$ can be considered large enough. As Landau states "In compression or expansion, as in any rapid change of state, the fluid ceases to be in thermodynamic equilibrium, and internal processes are set up in it which tend to restore this equilibrium. These processes are usually so rapid (i.e. their relaxation time is so short) that the restoration of equilibrium follows the change in volume almost immediately unless, of course, the rate of change of volume is very large."(cit) [7]. This is clearly valid for a stationary case, but it is important to consider that in case of a disruption the volume rate of change is quite big and the term might not be neglegible.

Otherwise, considering a low or null velocity field

$$\nabla\cdot\overline{v} = 0 \xrightarrow{yields} \tau_{ij} = -p\delta_{ij} + \mu\left(\frac{\partial v_i}{\partial x_i} + \frac{\partial v_i}{\partial x_i}\right)\ where \begin{cases} i = j \ \rightarrow \delta_{ij} = 1 \\ i \neq j \ \rightarrow \delta_{ij} = 0 \end{cases} \tag{2.20}$$

$$\tau_{xx} = -p + 2\mu\frac{\partial u}{\partial x} \tag{2.20A}$$

$$\tau_{yy} = -p + 2\mu\frac{\partial v}{\partial y} \tag{2.20B}$$

$$\tau_{zz} = -p + 2\mu\frac{\partial w}{\partial z} \tag{2.20C}$$

$$\tau_{xy} = \mu\left(\frac{\partial u}{\partial y} + \frac{\partial v}{\partial x}\right) \tag{2.20D}$$

$$\tau_{xz} = \mu\left(\frac{\partial u}{\partial z} + \frac{\partial w}{\partial x}\right) \tag{2.20E}$$

$$\tau_{yz} = \mu\left(\frac{\partial v}{\partial z} + \frac{\partial w}{\partial y}\right) \tag{2.20F}$$

Contributes (2.20A-F) can be further divided in matrix form as

$$\underline{\underline{\Pi}} = \underline{\underline{\Pi_s}} + \underline{\underline{\Pi_D}} = \begin{bmatrix} p & 0 & 0 \\ 0 & p & 0 \\ 0 & 0 & p \end{bmatrix} + \begin{bmatrix} 2\mu\dfrac{\partial u}{\partial x} & \mu\left(\dfrac{\partial u}{\partial y} + \dfrac{\partial v}{\partial x}\right) & \mu\left(\dfrac{\partial u}{\partial z} + \dfrac{\partial w}{\partial x}\right) \\ \mu\left(\dfrac{\partial u}{\partial y} + \dfrac{\partial v}{\partial x}\right) & 2\mu\dfrac{\partial v}{\partial y} & \mu\left(\dfrac{\partial v}{\partial z} + \dfrac{\partial w}{\partial y}\right) \\ \mu\left(\dfrac{\partial u}{\partial z} + \dfrac{\partial w}{\partial x}\right) & \mu\left(\dfrac{\partial v}{\partial z} + \dfrac{\partial w}{\partial y}\right) & 2\mu\dfrac{\partial w}{\partial z} \end{bmatrix} \tag{2.21}$$

And the Eulerian’s equation under a lagrangian form can be written, previously modifying the stress tensor $\underline{\underline{\Pi_D}} = -\underline{\underline{\Pi_\nu}}$, as

$$\rho \frac{Du}{Dt} = -\nabla \cdot \left(\underline{\underline{\Pi_s}} - \underline{\underline{\Pi_\nu}} \right) + \rho \underline{g} = -\nabla \cdot \left(p\underline{\underline{I}} - \underline{\underline{\Pi_\nu}} \right) + \rho \underline{g} = -\nabla \mathrm{p} + \nabla \cdot \underline{\underline{\Pi_\nu}} + \rho \underline{g} \tag{2.22}$$

2.4 Fluid-Structure Interaction (FSI)

This FSI interaction involves three different components of varying importance: pressure and viscous forces acting on the solid boundary; VV deformation that changes the conformation of the fluid domain and, last but not least, the fluid reacting to the structure movement, which imposes a velocity on the fluid-solid boundary.

COMSOL proposes two different type of solver for a FSI problem, one of which is defined “fully coupled” solver and follows the monolithic approach; this consists in simultaneously solving the equations governing the fluid flow, the structure displacement and exerted forces in a single solver.

The problem can then be discretized in general terms with the matrix [8]

$$\begin{bmatrix} \underline{\underline{K_s}} & \underline{\underline{K_{fs}}} \\ \underline{\underline{K_{sf}}} & \underline{\underline{K_f}} \end{bmatrix} \cdot \begin{bmatrix} \underline{u_s} \\ \underline{u_f} \end{bmatrix} = \begin{bmatrix} \underline{F_s} \\ \underline{F_f} \end{bmatrix} \tag{2.23}$$

where $\underline{u}$ provides an information about the motion of the fluid or of the structure, $\underline{F}$ represents the exerted forces between these two and $\underline{\underline{K}}$ represent a stiffness term that links the previous terms and depends on the material properties. The use of a solver with a “fully coupled” approach ensures the advantage of stability while accelerating convergence at the same time.

2.5 Two-dimensional model

It is possible now to further reduce the system of equations presented above in the case of a generic two-dimensional geometry, thus obtaining from the Hooke’s Law and the NS system the final formulations that will be used, along with analytical closed form equations, for the static validation of the model. In detail, stresses along the entire geometry will be compared with Lamè equations while the Archimede’s law applied to an immersed body will be used as a term of comparison for the Lift force obtained with Comsol.

2.5.1 Mechanical formulation for a two-dimensional model

The stress and deformation field on a thick cylinder, represented by a ring under plane stress conditions, can be obtained with the Lamè equations. We can thus calculate them in the radial and tangential direction, defining the radial stress σ_r and the hoop stress σ_θ, leading to

$$\sigma_r = \frac{E}{1-\nu^2}\left[C_1(1+\nu) - C_2\left(\frac{1-\nu}{r^2}\right)\right] \tag{2.24}$$

$$\sigma_\theta = \frac{E}{1-\nu^2}\left[C_1(1+\nu) + C_2\left(\frac{1-\nu}{r^2}\right)\right] \tag{2.25}$$

$$\varepsilon_r = \frac{1}{E}(\sigma_r - \nu\sigma_\theta) \;\; ; \;\; \varepsilon_\theta = \frac{1}{E}(\sigma_\theta - \sigma_r) \tag{2.26}$$

Where C1 and C2 constant can be obtained introducing the boundary conditions $\sigma_r(r_i) = 0;\ \sigma_r(r_o) = -P_o$ Introducing the latest inside the stress equations we can obtain the following

$$\sigma_r = \frac{r_i^2 P_i - r_o^2 P_o}{r_o^2 - r_i^2} - \frac{(P_i - P_o) r_i^2 r_o^2}{(r_o^2 - r_i^2) r^2} \tag{2.27}$$

$$\sigma_\theta = \frac{r_i^2 P_i - r_o^2 P_o}{r_o^2 - r_i^2} + \frac{(P_i - P_o) r_i^2 r_o^2}{(r_o^2 - r_i^2) r^2} \tag{2.28}$$

As previously proposed, under plane stress hypotesis we can then use the Hooke's law to tie stress tensor components to deformations

$$\begin{bmatrix} \varepsilon_{xx} \\ \varepsilon_{yy} \\ 2\varepsilon_{xy} \end{bmatrix} = \frac{1}{E} \begin{bmatrix} 1 & -\nu & 0 \\ & 1 & 0 \\ symm & & 2(1+\nu) \end{bmatrix} \cdot \begin{bmatrix} \sigma_{xx} \\ \sigma_{yy} \\ \sigma_{xy} \end{bmatrix} \tag{2.29}$$

2.5.2 Fluid dynamic formulation for a two-dimensional model

In this case the (2.21) equations can be written as

$$\underline{\underline{\Pi}} = \underline{\underline{\Pi_s}} - \underline{\underline{\Pi_v}} = \begin{bmatrix} p & 0 \\ 0 & p \end{bmatrix} - \begin{bmatrix} 2\mu\dfrac{\partial u}{\partial x} & \mu\left(\dfrac{\partial u}{\partial y} + \dfrac{\partial v}{\partial x}\right) \\ \mu\left(\dfrac{\partial u}{\partial y} + \dfrac{\partial v}{\partial x}\right) & 2\mu\dfrac{\partial v}{\partial y} \end{bmatrix} \tag{2.30}$$

And this one can be introduced in the integral form of the momentum equation in just few more passages

$$\int_{Sys} \frac{D(\rho\underline{u})}{Dt} = \oint_{\delta\Omega} \frac{\partial(\rho\underline{u})}{\partial t} dA + \oint_{\delta\Omega} (\rho\underline{u})\underline{u} \cdot \underline{n} dA + \int_{\Omega} \rho\underline{g} dV = -\int_{\delta\Omega} \left(p\underline{\underline{I}} - \underline{\underline{\Pi_\nu}}\right) \cdot \underline{n} dA + \int_{\Omega} \rho\underline{g} dV \tag{2.31}$$

The (2.31) equation leads to the definition of the Drag and Lift force as a projection on the main axis of the force D defined as

$$\underline{F} = -\oint_{\delta\Omega} \left(p\underline{\underline{I}} - \underline{\underline{\Pi_\nu}}\right) \cdot \underline{n} dA + \int_{\Omega} \rho\underline{g} dV = -D \xrightarrow{yields} D = \oint_{\delta\Omega} p\underline{\underline{I}} \cdot \underline{n} dA - \oint_{\delta\Omega} \underline{\underline{\Pi_\nu}} \cdot \underline{n} dA \tag{2.32}$$

Both static and dinamic model use these two concepts intensively, and their formulation can be further simplified for known geometries: supposing a ring immersed in a fluid under a variable velocity field (Fig.5) the terms deriving directly from the (2.32) equation can be expressed as

$$D(t) = \oint dF_x = -\oint pcos\theta dA + \oint \tau_w sin\theta dA \qquad (2.33)$$

$$L(t) = \oint dF_y = -\oint psin\theta dA + \oint \tau_w cos\theta dA \qquad (2.34)$$

To simplify the reading, only the decomposition of the drag term is now proposed. Considering a different geometry example this can be written as

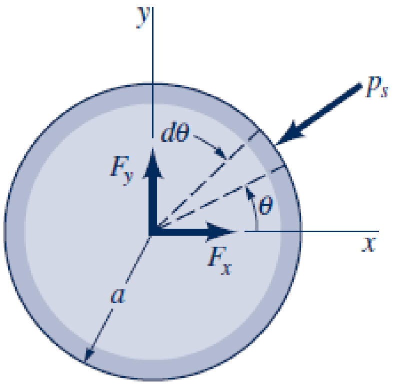

Fig. 5 - Ring subjected to Drag and Lift forces

$$D(t) = \oint dF_x = \oint p \cdot \underline{n_{x,w}} dA - \oint \underline{\tau_{x,w}} \cdot \underline{n_{x,w}} dA \qquad (2.35)$$

Or else

$$D(t) = \oint dF_x = \oint p \cdot n_w dA - \oint \mu\left(2\tau_{xx,w} \cdot n_{x,w} + \tau_{xy,w} \cdot n_{y,w}\right) dA$$

$$\xrightarrow{yields} D(t) = \oint dF_x = \oint p \cdot n_w dA - \oint \mu \left(2\frac{\partial u}{\partial x} \cdot n_{x,w} + \left(\frac{\partial u}{\partial y} + \frac{\partial v}{\partial x}\right) \cdot n_{y,w}\right) dA \qquad (2.36)$$

As the above (2.36) finally shows, the force term is made up of two components: a pressural one, found both on a stationary or time dependent kind of analysis, and a viscous one that entirely relies on the fluid velocity gradient depending on dinamic viscosity. Therefore, from a static analysis point of view of a ring immersed in a fluid, only the pressure term matters, generating a positive lift force, while the drag one is equal to zero. The lift force for this geometry,consequently, can be easily compared with a close form equations as the Archimede's Law one.

2.5.3 Resolution algorithm

It is now appropriate to present a conceptual scheme that summarizes the mathematical procedure used so far (Fig.6).

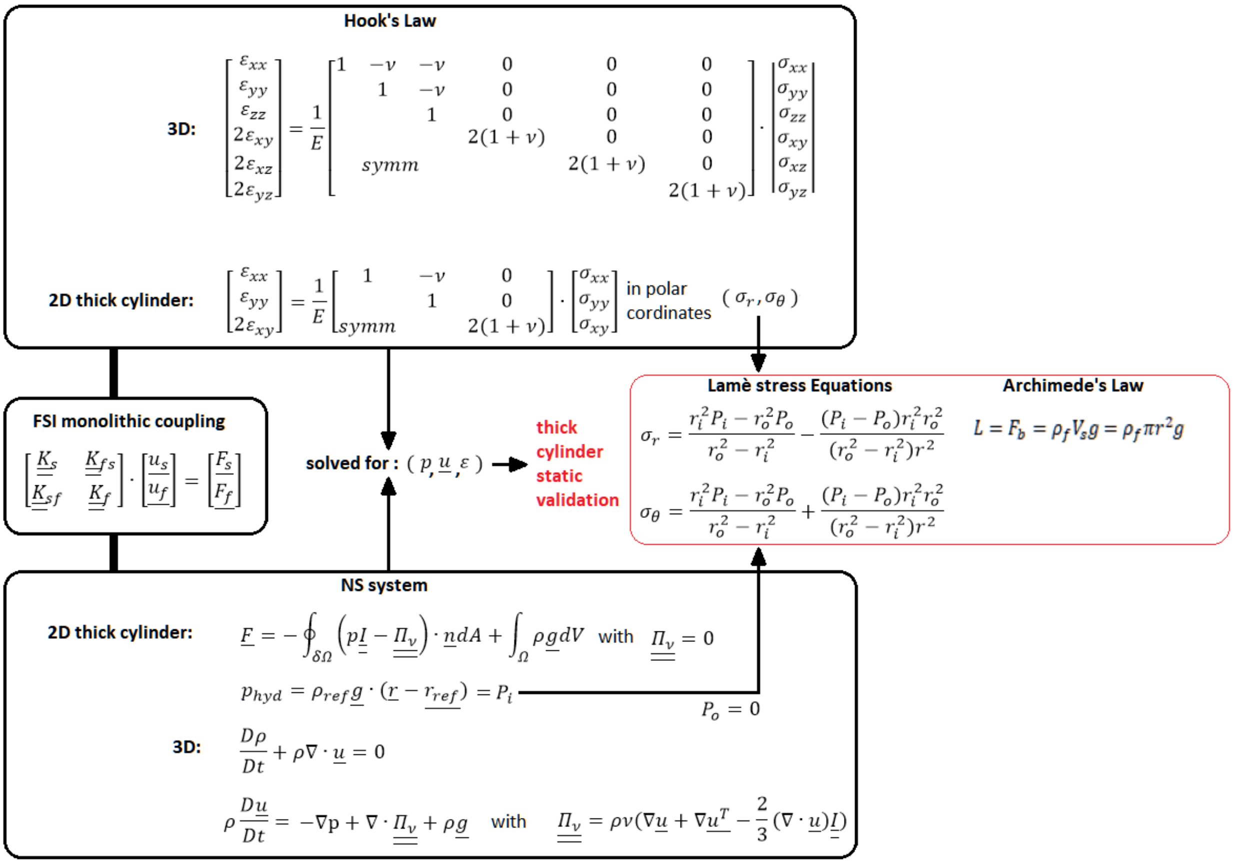

Fig. 6 - Conceptual recap of the Mathematical procedure used

As shown, equations of the NS system, Hooke's law and the FSI coupling algorithm used by COMSOL to provide the solution in a mechanical/CFD type of analysis were firstly defined for a generic three-dimensional geometry. These are usually solved for $(p, \underline{u}, \varepsilon)$ term and all of the consequent quantities, as stress along the geometry or mutual exerted forces between the vessel and the blanket, can be derived by knowing their fields.

These equations were then reduced to their bi-dimensional equivalent and applied on a geometry simple as a thick cylinder subjected to a constant external pressure, in order to compare the results provided by the software with analytic closed-form equations suitable for stationary cases. In this model the stress configuration was obtained as Hoop and radial distributions and validated using Lamè equations while forces exerted on the vessel, reduced now to the lift alone, were compared with the Archimede's Law.

Geometry was then upgraded to the "real" vessel/tank couple one's and revolved around its axial direction. This last model, by means of the equations explained above, was then analyzed from a dynamic point of view of a simulated impact due to a disruption.

As already mentioned, the FEM analysis was carried out using the COMSOL software while the analysis of the signals supplied by it was carried out with the aid of the Matlab software.

COMSOL Multiphysics is a FEM (Finite Element Model) software capable of solving 2D and 3D PDEs (Partial Differential Equations) in single physic and multiphysics simulation tasks. It is integrated with a geometry building tool that allows the definition of object sub-entities to ensure a proper meshing, other than an easy parametrization of the object physical quantities. COMSOL has several modules available for a vast range of applications, categorized according to the applications areas of Electrical, Mechanical, Fluid, Acoustic, Chemical, Multipurpose, and Interfacing [9].

The previous mechanic and fluid dynamic equations and all of the boundary conditions were integrated inside the mechanical and CFD comsol module.

Matlab is a high performance language and a numerical computing environment that, among other things, allows the user to easily import datasheets from other programs and process them for a further analysis.

In this work MATLAB has been mainly used for plotting equations and parameters range of values and for post-processing purposes of comsol time dependent datas.

2.6 Boundary conditions

In order to achieve proper modelling results, different boundary conditions for stationary and dynamic side analysis have been checked and the most suitable ones have been choosed for the final model.

Regarding the stationary model the fixed constraint was used as a mechanical constraint for VV structure; the inner vessel volume wasn't modelled, supposing it is mainly vacuum, while the VV-blanket interface was modelled as a no-slip wall with FSI analysis enabled. The fluid coating was modelled as a simple FLiBe tank with simple no-slip wall conditions on the outer boundaries except the upper one, where an open boundary condition was used to ensure the proper mass flow of FLiBe to fill the volume left by deformations. More specifically, the open boundary condition was set in order to let the fluid enter/exit the tank while the structure stabilizes its geometry under mechanical and pressure loads.

The dynamic model is practically composed of the same boundary conditions as the previous one, except for the upper tank wall that is a no-slip wall condition too. In fact, the output provided by the stationary model was placed as initial condition for the dynamic one, in order to begin the disruption transient with a dynamically stabilized system. The no-slip wall upper boundary condition, based on these pre-conditions, ensures the conservation of the fluid mass in the tank-vessel system, what besides guarantees that fluid-wall interaction effects in the upper area can be correctly taken into account.

As far as the no-slip wall condition is concerned, this exists where the fluid velocity relative to the wall velocity is zero; that means clearly that if the wall velocity is zero $\underline{u_f} = \underline{u_{tr}} = 0$. It basically represents the presence of a boundary layer due to the viscous effects.

The open boundary condition, as previously stated, allows an exchange of mass and describes boundaries in contact with a large volume of fluid. Then, the normal stress setting implicitly imposes $p = f_0$ and, if the hydrostatic pressure option is enabled, the term is automatically added to the pressure entered in f_0 input, in our case equal to zero. The equations used can so be represented as

$$\left[-p\underline{\underline{I}} + \underline{K}\right] \cdot \underline{n} = -\left(f_0 + p_{hyd}\right) \cdot \underline{n} \;\; and \;\; p_{hyd} = \rho_{ref}\,\underline{g} \cdot \left(\underline{r} - \underline{r_{ref}}\right) \qquad (2.47)$$

From a vessel constraint point of view the fixed constraint condition makes the geometry fixed, simply setting displacements equal to zero in all directions or, in other words, setting the velocity of the solid in the point/boundary as $\underline{u_s} = 0$

Finally, as previously shown in the Disruption chapter, modeling a disruption is not an easy task: the configuration of exerted electromagnetic forces by thermal and current quench is not evenly distributed along the vessel internal surface and is heavily influenced by the load point position. Moreover, different material properties should be considered for the vessel structural layers and their boundary interface properties should be properly taken into account in the model definition. The complexity of the argument led then to the assumption of simulating a disruption with a Gaussian pulse load condition, initally considered at the exact geometrical center of the vessel belly and directed radially as $\underline{F} = F_x$.

The aim of this work is in fact providing a modelling strategy for the vessel-blanket interaction to show that the model can be used for further analysis on a disruption event management, but future papers should absolutely concentrate on a proper definition of the electromechanical distribution to provide a quantitative model.

Chapter 3

3 Two-dimensional model validation

3.1 Material Properties

Physical and fluid dynamic properties behaviour of FLiBe’s liquid form is, throughout the litterature regarding the argument, fairly uniform. One of the most truthful trends for density and dinamic viscosity can be derived from the equations proposed by Cantor (1979) and Cantor et. Al (1969) [10]:

$$\rho\left[\frac{kg}{m^3}\right] = 2413.03 - 0.4884 * T[K] \quad T\epsilon[788 - 1094] \tag{3.1}$$

$$\nu\,[Pa * s] = 0.0000249 * 10^{\frac{1944}{T[K]}} \quad T\epsilon[800 - 1050] \tag{3.2}$$

The two boxes highlight the properties variation range which, in any case, remains rather limited between the values 800-870 K.

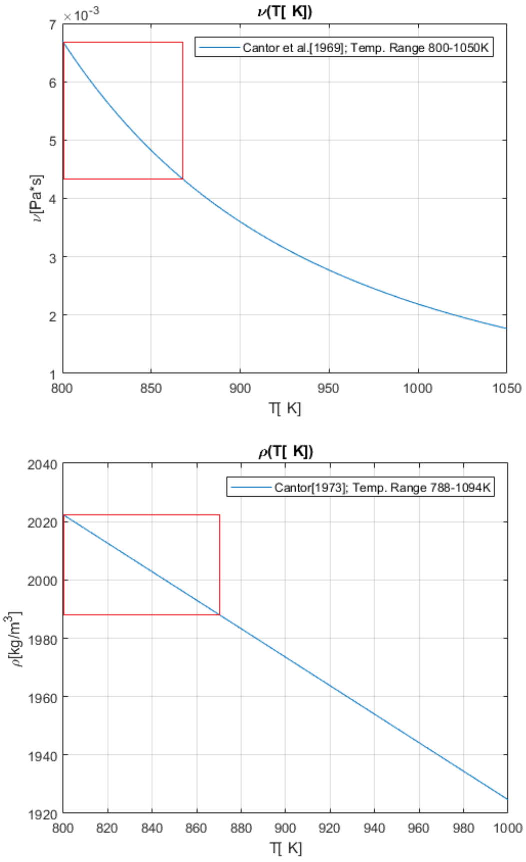

Fig. 7 - Density and Dinamic viscosity trend as a function of temperature

Density has a linear decrease within this temperature range, starting from 2020 [kg/m^3] at 800 K; most of the outer vessel cooling circuit stands anyhow above the lower limit (around 800 K) and the internal circuit is the only one with a density variation remotely significant for the purpose of a first CFD evaluation of the vessel behaviour. The dinamic viscosity coefficient, on the other hand, has a very low value (comparable to the water's one) and even an exponential trend is not enough to justify studies on this quantity variation.

As a first approximation, for the above given reasons and to the purpose of mechanical modelling, both the FLiBe structure layer and the blanket can be considered around 850 K.

The Inconel 718 properties are tabulated and well known for different temperatures, and even if the vessel is far from having a uniform temperature along its geometry and along its thickness, it was decided to consider the structure at the same temperature of the blanket: the approximation proved to be necessary in order to not excessively complicate the model, which otherwise would have showed a significant increase in the resolution time.

Because of all the above mentioned, the following material properties can be derived for the structure and the blanket:

FLiBe Blanket	$\rho\left[\frac{kg}{m^3}\right]$	Dinamic viscosity $\nu\ [Pa*s]$		
	2000	0.1267		
Inconeln 718	$\rho\left[\frac{kg}{m^3}\right]$	Poisson's Ratio ν	E [Gpa]	Rp 0.2% [MPa]
	8150	0.2715	160	700

Table 1 - Assumed values for material properties

3.2 Model of a ring under stationary conditions

It is now appropriate to proceed showing the results provided by the software for the thick cylinder, represented by a ring under plane stress conditions, subject to a constant external pressure. The solution, provided as $(p, \underline{u}, \varepsilon)$ fields, was further processed to obtain radial σ_r and hoop σ_θ stress tensor distribution (Fig.8).

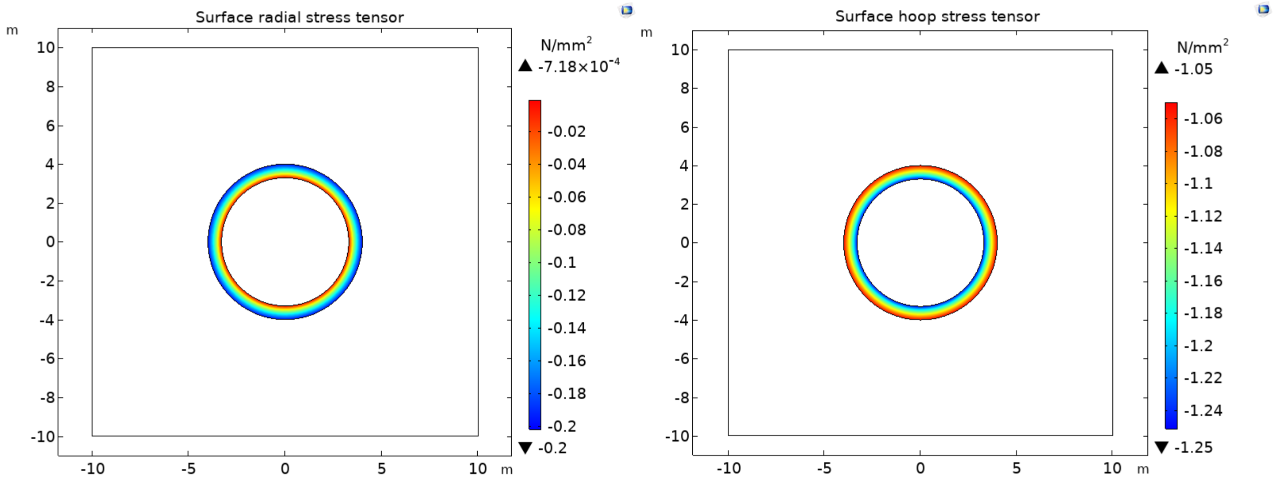

Fig. 8 - COMSOL plots of surface radial stress tensor and surface hoop stress tensor

Therefore, considering a radius of 4 m, a ring thickness of 0.7 m and a simple model with an uniform pressure of 2 bar, the stress analytical results shown in Fig.9 are well represented in the model stationary behaviour. The use of a fine mesh size produced a well converged model with a good agreement with analytical results of Fig.8, characterized by an error on the stress less than 0.01 N/mm^2(MPa).

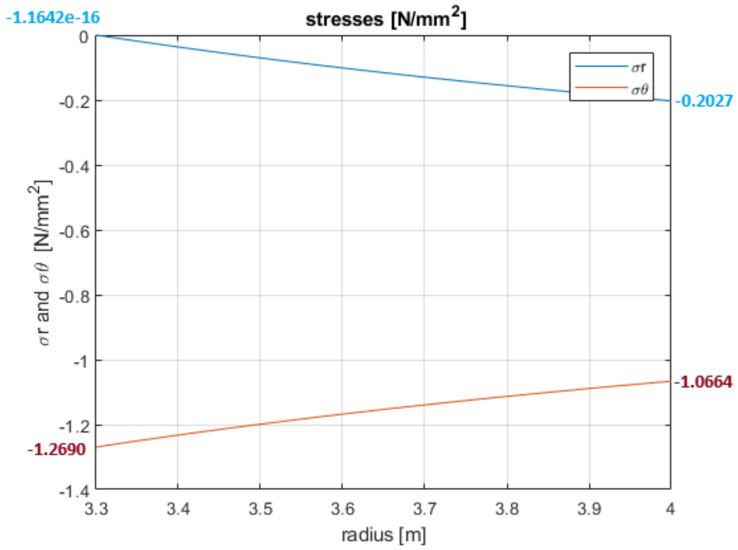

Fig. 9 - Analytical results for Lamè equations

A second CFD model was built considering the hydrostatic pressure to investigate strain and stresses due to lift effects on the structure (Fig.10).

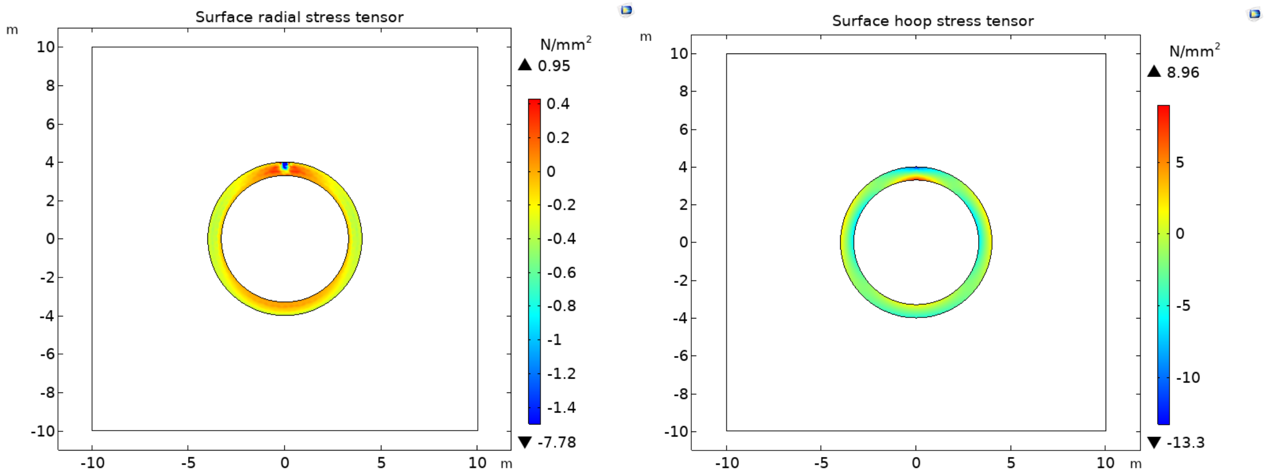

Fig. 10 - COMSOL stress tensors results for a thick cylinder under hydrostatic pressure

Considering a rigid domain, the lift force on an immersed body can simply be calculated with the Archimede's law $L = F_b = \rho_f V_s g = \rho_f \pi r^2 g = 9{,}8571 * 10^5\ N/m$. With comsol, considering the velocity field equal to zero and a rigid domain, applying the aforementioned equation for each pressure value of the nodes, the result value of the equation is $L = \oint dF_y = \oint p \cdot n_y dA = 9{,}8567 * 10^5\ N/m$ obtaining a value near to analitycal one with an error of 0.001*$10^5\ N/m$. The value calculated with a single fixed constraint point actually shows discrepancies due to the finite mesh size and also to the fact that comsol takes into account the volume reduction of the blanket caused by induced deformations on the thick ring.

In addition, the stress field shows that lift forces, in the absence of a gravitational weight, compress the geometry on the upper punctual constraint. The constraint effectively locks the cylinder slice position inside the fluid tank and thus cancels the "theoretical buoyancy" of the vessel. It is also noteworthy that, around the region of the constraint, the action of bending moments produces a notable increase in the radial and hoop stress compared to the average stress value.

In the last model we added the gravity force to the ring to check if the model correctly computed the reaction forces and the derived stresses caused by the structure own weight (Fig.11)

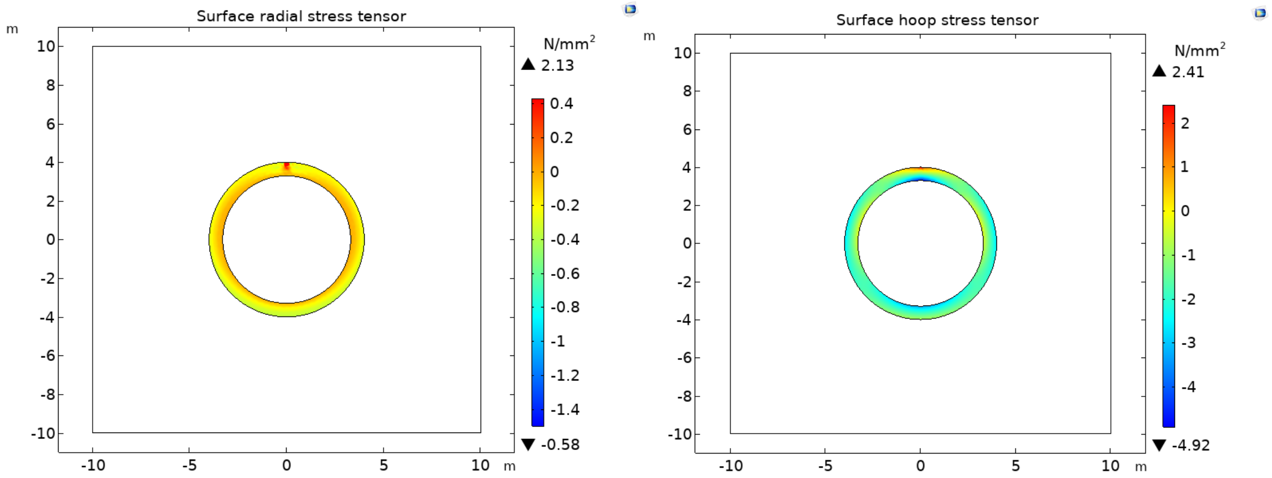

Fig. 11 - COMSOL stress tensor results for a thick cylinder under hydrostatic pressure and structure weight

As the figure show the stress is now concentrated on the point constraint because of the structure own weight. Comsol correctly computes the structure weight and the lift force presenting values similar to analytical ones (Tab.2).

	weight [N/m]	lift force [N/m]
Analytical results	-1.2892e6	9.8571e5
Comsol results	-1.2904e6 (error 0.01e6)	9.8516e5 (error 0.01e5)

Table 2 - Comparison between COMSOL and analytical results for The weight of the ring and the lift force applied on it

Chapter 4

4 Three-dimensional model

The 3D vacuum vessel model is simply derived from a plane rappresentation of the structure revolved around the z axis over 360°. This was decided to be a made of a single layer of Inconeln718 with a thickness of 70mm, due to the complexity of the model and to the computing time request that the model would have taken if a multi-layer analysis with different materials had been conducted. The same procedure was then followed for the fluid blanket, modeled as a fixed tank geometry where the external wall behaviour was not simulated, and a bland corner smoothing operation was performed to avoid pressure and velocity field singularities.

4.1 Meshing

In general terms creating a suitable mesh is crucial for avoiding error and mesh warning as well as ensuring to obtain proper results.

In this work, on the other hand, a suitable mesh has been critical for reducing computation times for the model since the physical behaviour of the structure has been analyzed under a qualitative point of view.

The software has a built in auto-meshing function that can be set in size and adjusts the mesh based upon the physics involved, materials properties, geometry and even boundary conditions within the physics [11] ensuring that all criteria for accurate results are achieved; the PC configuration used for the analysis however was often not enough powerful to get results with finer meshes because of the out of memory error that would appear both in the stationary and the time dependent analysis.

For this reason, a custom meshing process have been used on the model, ensuring that custom build results were acceptable in comparison to the ones derived from the auto-meshed model (assumed to be the preferred one). Comparison terms used for meshes are provided by COMSOL as mesh quality measures: Skewness, Maximum angle, Volume versus circumradius, Volume versus length, Condition number and Growth rate. All of quality measures reside in the 0-1 range, where value 1 indicates the best possible quality and an optimal element and, on the contrary, value 0 indicates that a mesh element geometry is degenerated. In general all elements below a quality of 0.1 will be considered poor-quality elements and COMSOL, in addition, automatically presents a warning in the mesh builder log if the quality element goes below 0.01 [12].

It is appropriate to present now a short explanation of the citated quality measures

- **Skewness**

  This quality measure is based on the equiangular skew defined as the minimum of the quantity $1 - \max(\frac{\theta-\theta_e}{180-\theta_e}, \frac{\theta_e-\theta}{\theta_e})$ where θ is the angle over a vertex (2D) or edge (3D) in the element, θ_e is the angle of the corresponding edge or vertex in an ideal element, and the minimum is taken over all vertices (2D) or edges (3D) of the element [13]. This measure penalizes elements with large or small angles as compared to the angles in an ideal element.

- **Maximum angle**

  The Maximum angle measure is based on the largest angle in an element. If no angle is larger than the largest angle of the corresponding optimal element, the quality is one; otherwise, the measure shows how much larger the angle is. [13] That highlights elements with large angles, making this option particularly well suited for meshes where anisotropic elements are desired.

- **Volume versus circumradius**

  This is a measure based on a quotient of the element volume and the radius of the circumscribed sphere (or circle) of the element. This quality measure is sensitive to large angles, small angles, anisotropy and is a proper measure for triangular meshes in 2D and tetrahedral meshes in 3D where isotropic elements are desired [13].

- **Volume versus length**

  Volume versus length is a measure based on a quotient of element edge lengths and element volume. It is primarily sensitive to anisotropy [13].

- **Conditioning number**

  The conditioning number is a quality measure which is based on the element dimension divided by the condition number (in the Frobenius norm) of the matrix transforming the element to a reference element [13]. Usually, that is one of the most important measures taken into account to check the quality of a mesh.

- **Growth Rate**

  Lastly the Growth rate measure is based on a comparison of the local element size to the sizes of neighboring elements in all directions. Basically, it increases towords 1 in mesh regions where elements size is comparable and decreases in mesh regions where elements size differs consistently.

4.2 Custom mesh plots and statistics

The custom mesh was firstly built as a free triangular mesh on both the structure and the blanket in the cut plane defined by the positive side of the x-z plane. The size of the mesh was chosen to be coarser for the fluid domain and coarse for the vessel domain (Fig.12).

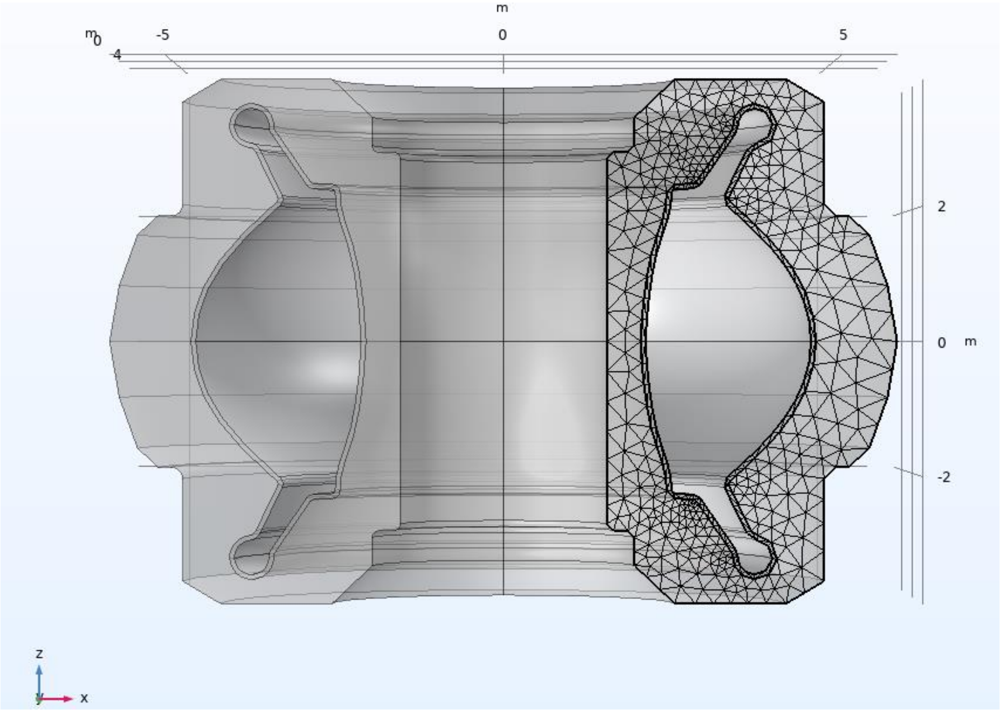

Fig. 12 - Free triangular mesh defined in X-Z plane

The mesh was then swept along 180 degrees with a normal size for the fluid domain and a fine size for the structure domain (Fig.13). The sweep mesh setting is extremely usefull whenever it is presumed that gradients of analyzed quantities are moderate along the sweep direction. Since our geometry is radially simmetrical we assume that stationary analysis quantities will be radially simmetrical too. It is furthermore supposed that in time-dependent analysis quantities as fluid pressure and velocity field gradients are moderate along the radial direction; this might be a strong assumption to make, but in our case it was necessary to achieve computation results in a decent amount of time.

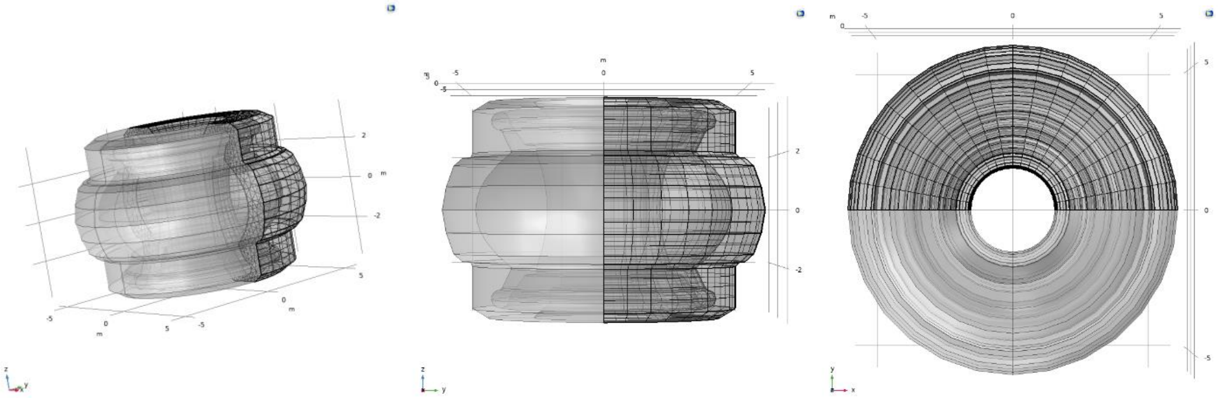

Fig. 13 - Sweep mesh operation on half of the geometry

The meshed domain, corresponding to a half of the final structure, was then copied on the other half of the entire geometry domain and a corner refine was then performed with the COMSOL given option (Fig. 14). Boundary layers options were then added to take into account the wall effect both on fluid-structure boundary layers and external blanket boundaries.

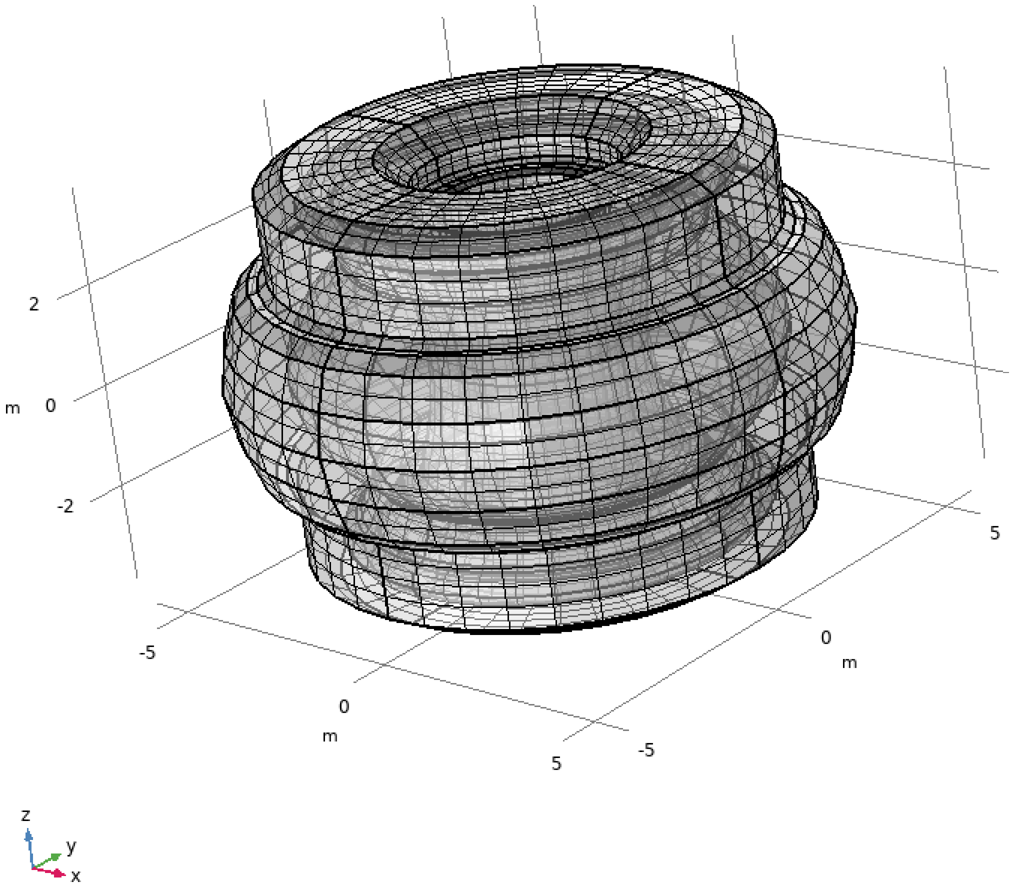

Fig. 14 - Mesh plot

The so constructed mesh can then be summarized by the table presented below (Tab.3).

Mesh elements statistics	Mesh vertices	Prisms	Hexaedra	Quads	Edge elements	Vertex elements
	28188	28656	11088	8640	3840	320
	Dofs (stationary)	Computing time (stationary)	Computing time (time-dependent)			
	287100	≃ 7m	≃6h			
Domain elements statistics	Number of elements	Element volume ratio	Mesh volume			
	39744	0.001888	388.8 m^3			

Table 3 - Statistics for the mesh used in the analysis

The minimum element quality and average element quality of the characterizing measures are then presented below (Tab.4).

	Skewness	Maximum angle	Volume vs. circumradius	Volume vs-length	Conditioning number	Growth rate
Minimum element quality	0.0061	0.2990	0.0117	0.0149	0.0722	0.2275
Average element quality	0.6347	0.7688	0.2355	0.3154	0.4224	0.6733

Table 4 - Quality measures statistics

The latter shows that the minimum element quality of four measures out of six are below the guard level. While the volume vs length might not be important since it is related to the anisotropy of the material (and we are considering a single layer of Inconel 718, an isotropic material) the other three measures (skewness, volume vs circumradius and conditioning number) should be increased to get more accurate result on elements below the 0.1 value.

Last but not least, the fluid domain was set as a deforming domain under the component definitions tab representing domains and boundaries where the mesh can deform. In this way a new mesh is not generated for each new configuration of the boundaries and the previous mesh is adapted perturbing mesh nodes so they conform with the moved boundaries [14].

4.3 Mesh comparison

It is finally possible to present the comparison adopted to show that the custom mesh used for the simulation, characterized by a lower quality compared to the physic based auto-mesh, is suitable for the analysis because it reveals the same qualitative behavior as higher quality meshes.

Results in 3 different cases of built mesh are below presented. The goal was clearly decreasing the DOFs (Degrees Of Freedom) of the model, in order to decrease aswell the computing time and the hard disk memory request, since 12 GB out of 16 GB of RAM were already used in almost every model used for the comparison.

The first mesh used was made with the auto-mesh setting and a coarse size for the elements (Fig. 15). This size was the only one permitted for the entire geometry because even a slight refinement led to multiple out of memory errors and the computation couldn’t succed.

The statistics for the mesh are (Tab. 5-6)

<table>
<tr>
<td><i>Auto-mesh</i> elements statistics</td>
<td>
<table>
<tr><td>Mesh vertices</td><td>Tetrahedra</td><td>Prisms</td><td>triangles</td><td>Edge elements</td><td>Vertex elements</td></tr>
<tr><td>90674</td><td>282833</td><td>72408</td><td>50546</td><td>8833</td><td>320</td></tr>
<tr><td>DOFs (stationary)</td><td>Computing time (stationary)</td><td>Computing time (time-dependent)</td><td></td><td></td><td></td></tr>
<tr><td>896638</td><td>≃11h 8m</td><td>Memory err.</td><td></td><td></td><td></td></tr>
</table>
</td>
</tr>
<tr>
<td>Domain elements statistics</td>
<td>
<table>
<tr><td>Number of elements</td><td>Element volume ratio</td><td>Mesh volume</td></tr>
<tr><td>355241</td><td>6.712e-4</td><td>390.4 m^3</td></tr>
</table>
</td>
</tr>
</table>

*Table 5- **Auto-mesh** statistics*

	Skewness	Maximum angle	Volume vs. circumradius	Volume vs. length	Conditioning number	Growth rate
Minimum element quality	0.0216	0.0346	4.184e-4	0.0300	0.0351	0.0620
Average element quality	0.6229	0.7321	0.5404	0.6290	0.6918	0.5708

*Table 6- **Auto-mesh** quality measures statistics*

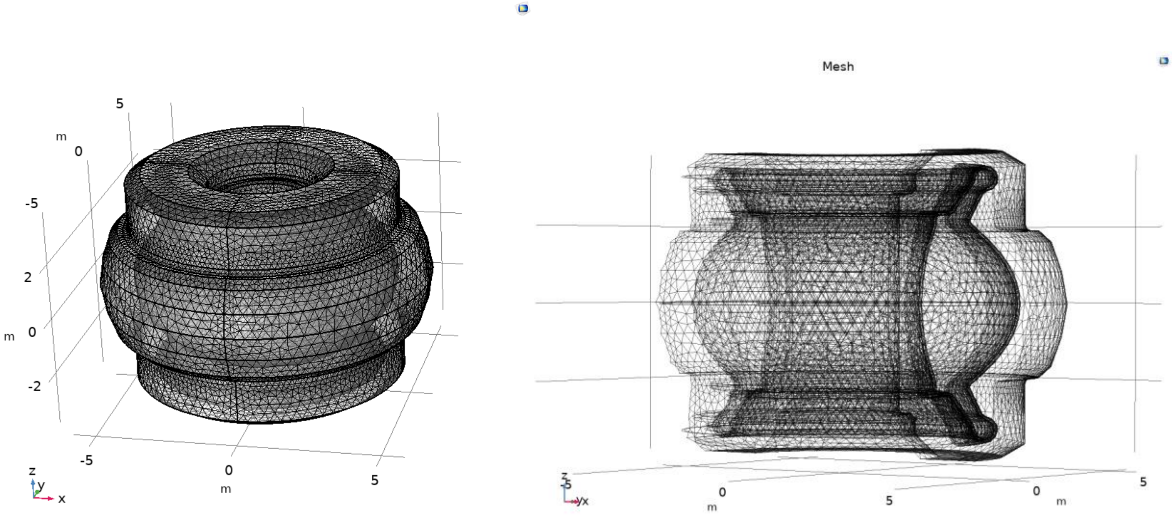

*Fig. 15 - Left: **Auto-mesh** plot for the entire geometry Right: **Auto-mesh** plot for half geometry*

Considering the great amount of time requested even by the stationary solver to solve the entire geometry, it was decided to use a slightly different version of the model for the stationary study. Assuming assialsymmetry conditions we modelled only a slice of the vessel-blanket couple and applied the periodic condition boundary on symmetry faces. This led us to an intermediate comparison model with slightly more DOFs than the previous one, and allowed even the use of a finer auto-mesh that fullfills almost all quality measures analyzed (except the volume vs circumradius one)(Fig 16). As stated in the previous chapter section, the relative tolerance plays also an important role on the computing time and relative tolerance for all of the previous models was set as 1e-3. In this case it was set as 1e-6 to ensure a good relative error even on derived parameters like stress distribution.

<table>
<tr><td rowspan="4"><i>Auto-mesh slice</i> elements statistics</td><td>Mesh vertices</td><td>Tetrahedra</td><td>Prisms</td><td>triangles</td><td>quads</td><td>Edge elements</td><td>Vertex elements</td></tr>
<tr><td>154921</td><td>666564</td><td>68470</td><td>56078</td><td>2042</td><td>3849</td><td>160</td></tr>
<tr><td>DOFs (stationary)</td><td>Computing time (stationary)</td><td></td><td></td><td></td><td></td><td></td></tr>
<tr><td>1456650+1(int)</td><td>≃ 10h 50m</td><td></td><td></td><td></td><td></td><td></td></tr>
<tr><td rowspan="2">Domain elements statistics</td><td colspan="2">Number of elements</td><td colspan="2">Element volume ratio</td><td colspan="3">Mesh volume</td></tr>
<tr><td colspan="2">735034</td><td colspan="2">5.877e-5</td><td colspan="3">32.49m^3</td></tr>
</table>

*Table 7 - **Auto-mesh slice** statistics*

	Skewness	Maximum angle	Volume vs. circumradius	Volume vs. length	Conditioning number	Growth rate
Minimum element quality	0.1361	0.1616	0.005	0.1659	0.2238	0.2668
Average element quality	0.6736	0.7583	0.6573	0.7334	0.7894	0.585

*Table 8 - **Auto-mesh slice** quality measures statistics*

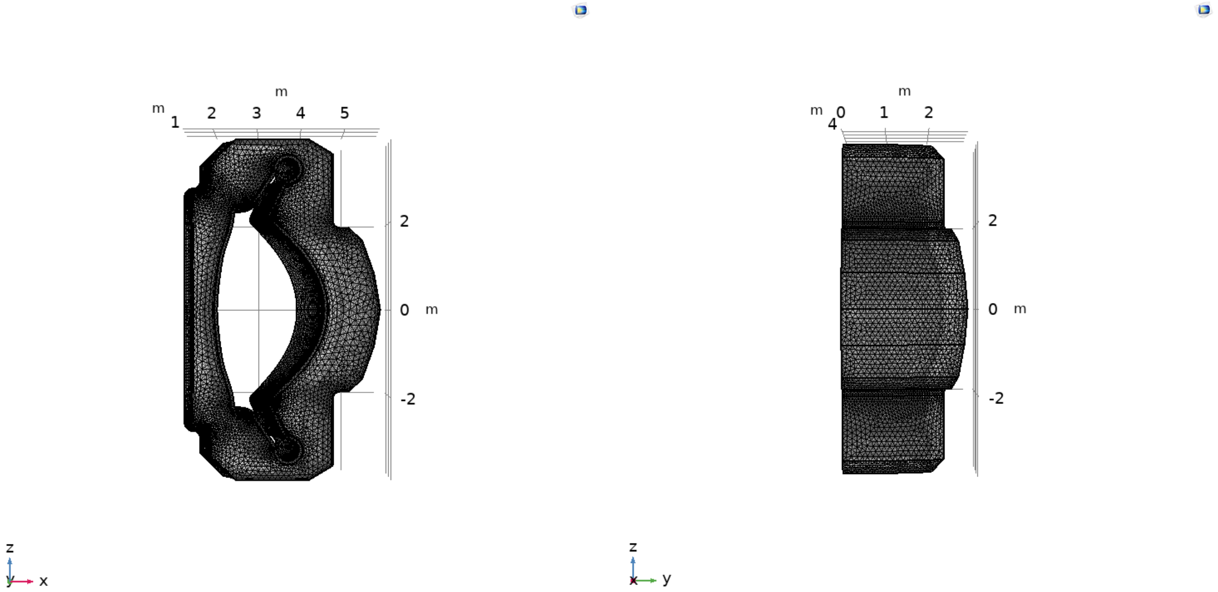

*Fig. 16 - Left: **Auto-mesh slice** plot for a slice of the entire geometry, X-Z plane Right: **Auto-mesh slice** plot for a slice of the entire geometry, Y-Z plane*

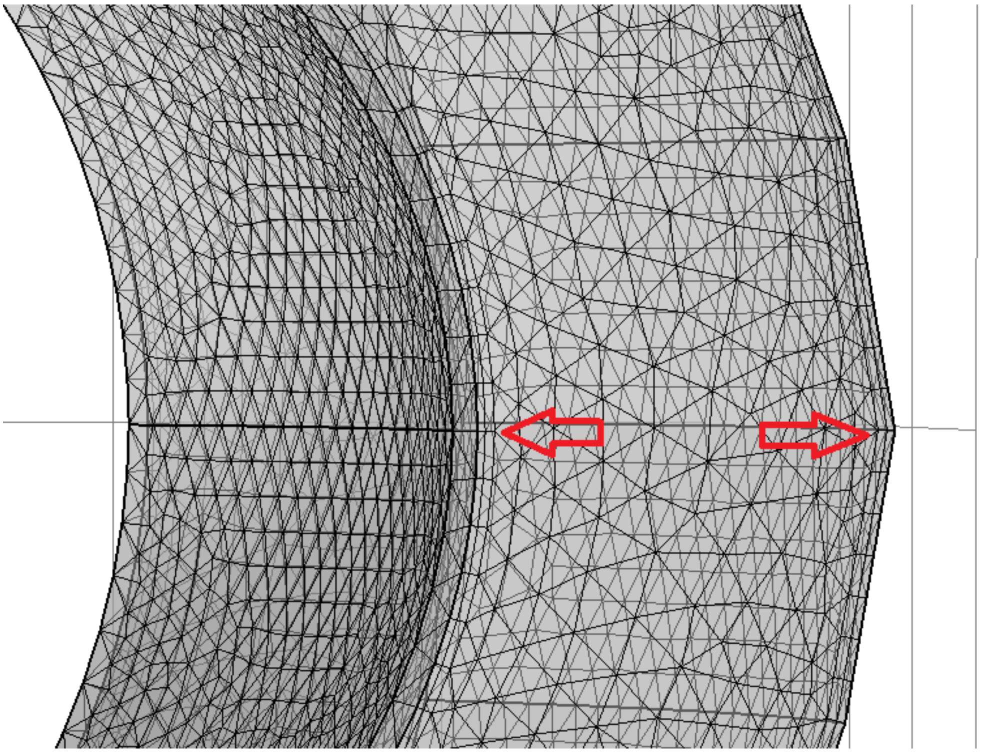

*Fig. 17 - **Auto-mesh slice**: detail of the boundary layers*

The third mesh, as previously presented, is modeled under the hypotesis that gradients of analyzed quantities are moderate along the sweep direction (Fig. 18). This mesh is the first step out of three custom meshes towards a compromise between the time intensive auto-mesh and the last custom mesh used (Fig.18-20) (Tab. 9-14).

Mesh 1 elements statistics	Mesh vertices	Prisms	Hexaedra	Quads	Edge elements	Vertex elements
	148224	174624	49152	36192	9188	320
	Dofs (stationary)	Computing time (stationary)	Computing time (time-dependent)			
	835612	≃ 9h 34m	> one week			

Domain elements statistics	Number of elements	Element volume ratio	Mesh volume
	223776	0.003622	389.9 m^3

*Table 9 - Custom **Mesh 1** statistics*

	Skewness	Maximum angle	Volume vs. circumradius	Volume vs. length	Conditioning number	Growth rate
Minimum element quality	0.1196	0.4235	0.08544	0.08983	0.1907	0.3879
Average element quality	0.7045	0.8137	0.4625	0.5839	0.6574	0.6903

*Table 10 - Custom **Mesh 1** quality measures statistics*

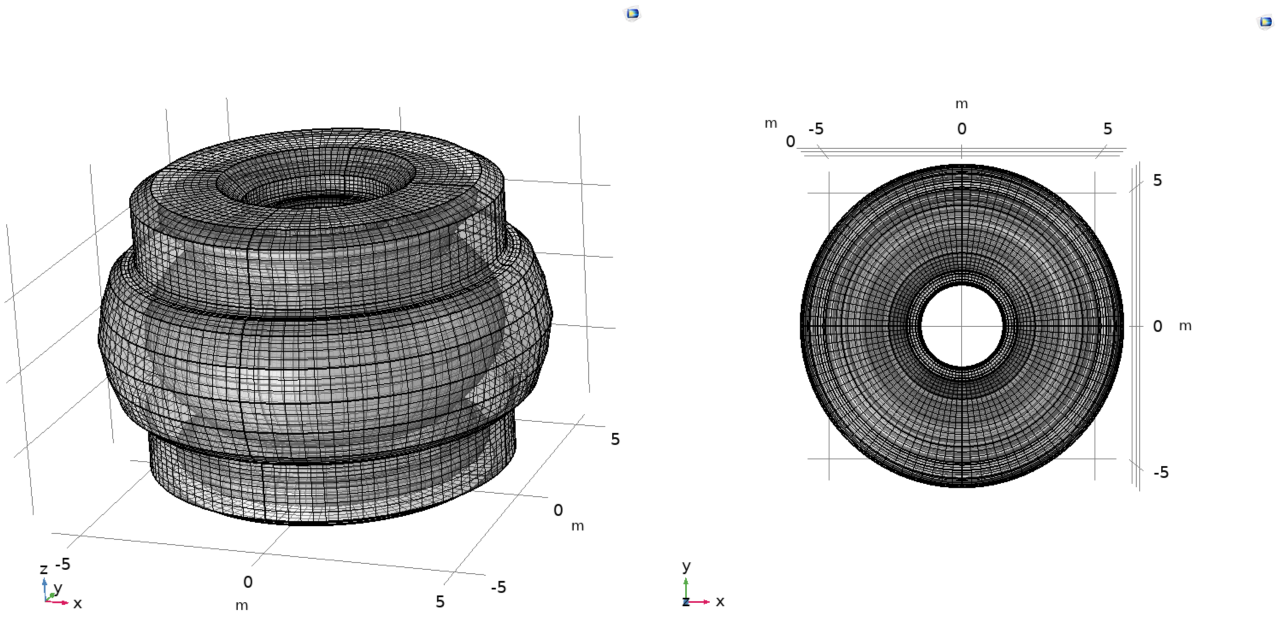

*Fig. 18 - Left: custom **Mesh 1** plot for the entire geomety Right: custom **Mesh 1** plot for the entire geometry, X-Y plane*

Mesh 2 elements statistics	Mesh vertices	Prisms	Hexaedra	Quads	Edge elements	Vertex elements
	41760	46944	14688	11304	4136	320

	Dofs (stationary)	Computing time (stationary)	Computing time (time-dependent)			
	409752	≃ 40m	≃4 days			

	Number of elements	Element volume ratio	Mesh volume
Domain elements statistics	61632	0.03724	388.4 m^3

*Table 11 - Custom **Mesh 2** statistics*

	Skewness	Maximum angle	Volume vs. circumradius	Volume vs. length	Conditioning number	Growth rate
Minimum element quality	0.0372	0.3604	0.0137	0.0143	0.0850	0.4007
Average element quality	0.6740	0.7896	0.1919	0.2626	0.3904	0.6808

*Table 12 - Custom **Mesh 2** quality measures statistics*

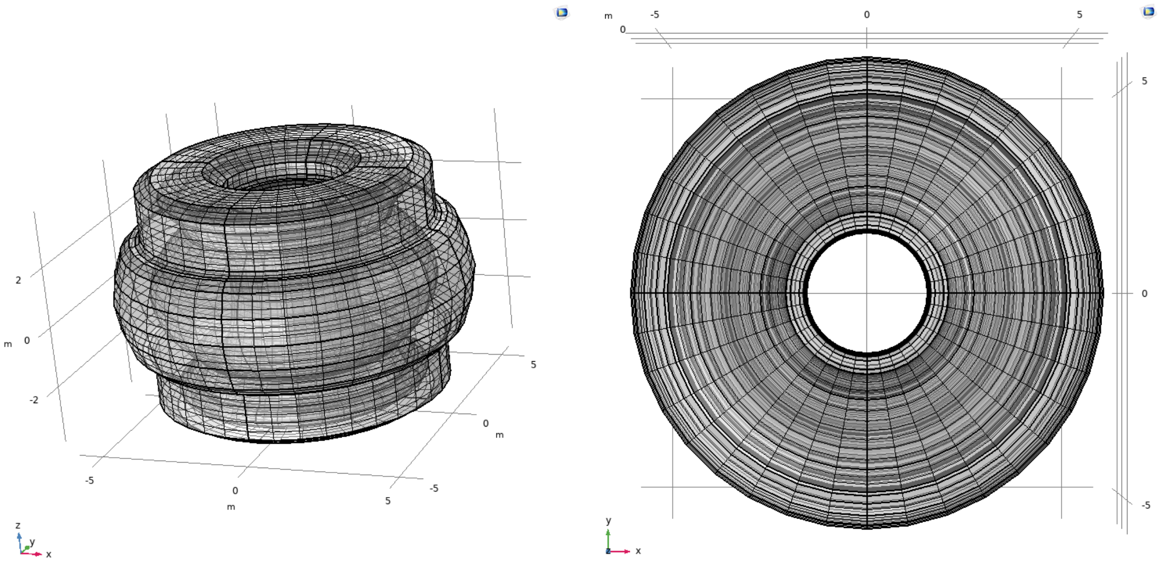

*Fig. 19 - Left: custom **Mesh 2** plot for the entire geomety Right: custom **Mesh 2** plot for the entire geometry, X-Y plane*

The last mesh presented is the one mainly used on the time dependent analysis and previously shown in detail with its histograms. It is now presented again just to simplify the comparison between the proposed meshes.

Mesh 3 elements statistics	Mesh vertices	Prisms	Hexaedra	Quads	Edge elements	Vertex elements
	28188	28656	11088	8640	3840	320
	Dofs (stationary)	Computing time (stationary)	Computing time (time-dependent)			
	287100	≃ 7m	≃6h			

	Number of elements	Element volume ratio	Mesh volume
Domain elements statistics	39744	0.001888	388.8 m^3

*Table 13 - Custom **Mesh 3** statistics*

	Skewness	Maximum angle	Volume vs. circumradius	Volume vs. length	Conditioning number	Growth rate
Minimum element quality	0.0061	0.2990	0.0117	0.0149	0.0722	0.2275
Average element quality	0.6347	0.7688	0.2355	0.3154	0.4224	0.6733

*Table 14 - Custom **Mesh 3** quality measures statistics*

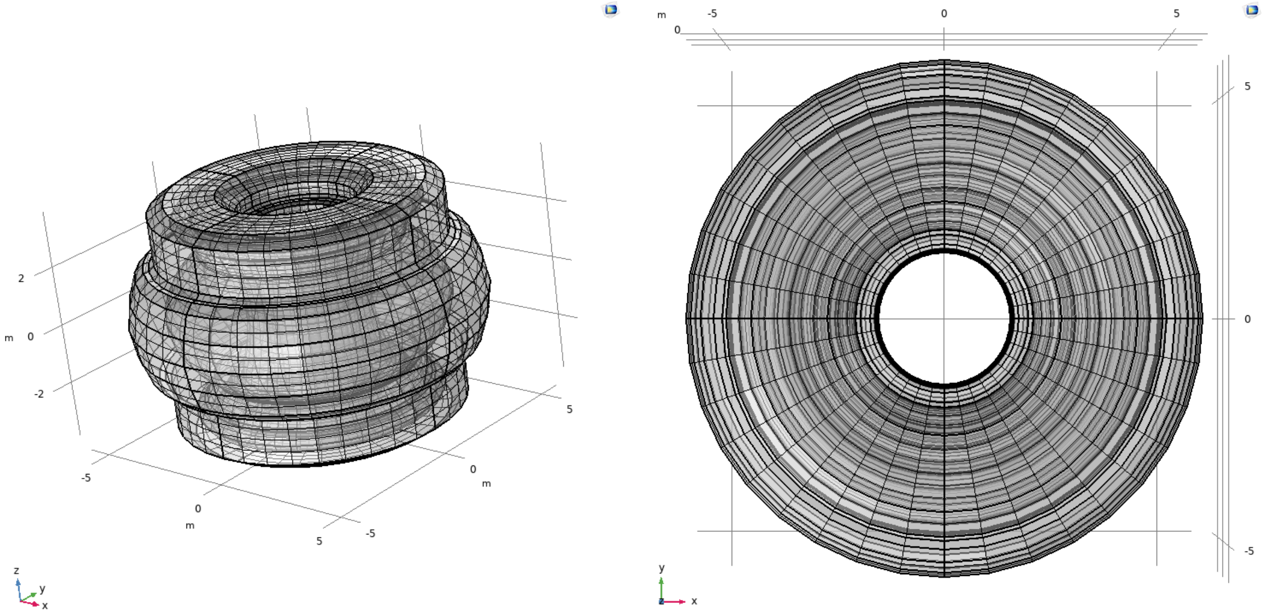

*Fig. 20 - Left: custom **Mesh 3** plot for the entire geomety Right: custom **Mesh 3** plot for the entire geometry, X-Y plane*

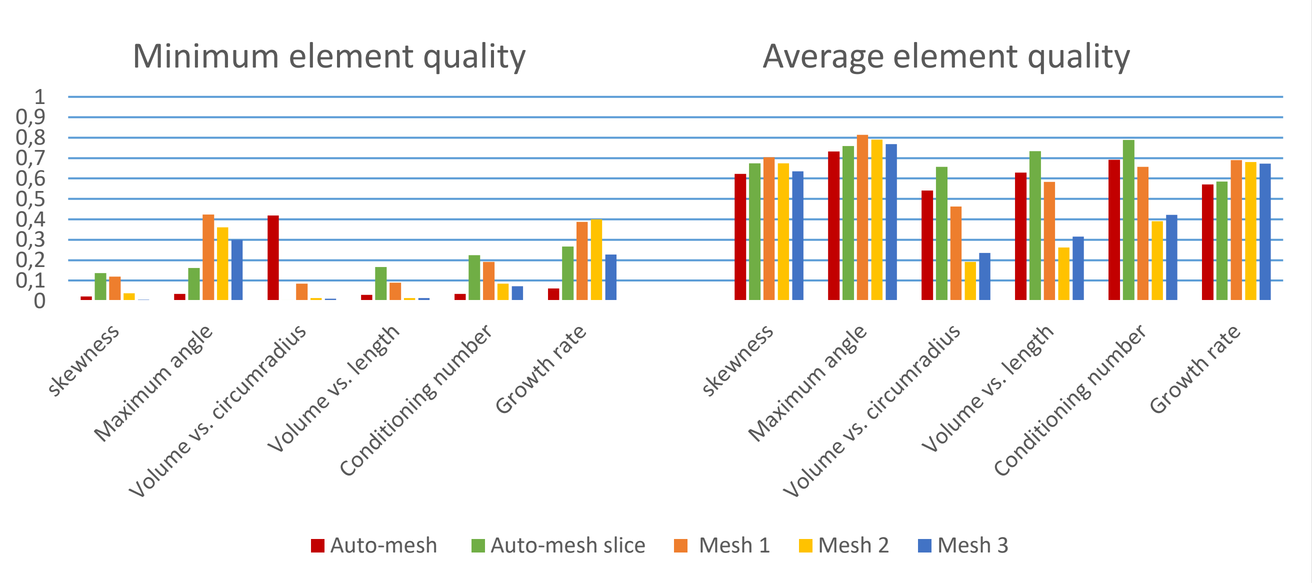

Fig. 21 - Hystograms of minimum and average element quality for the presented meshes

As the hystograms summarize in Fig. 21 *Auto-mesh* is characterized by a consistent number of minimal values below the 0.1 threshold and in fact an error regarding domain regions thinner than the specified minimum element size is presented during the mesh building. Moreover, average values of element quality are comparable to other custom mesh, meaning that the built-in meshing program (set to use a coarse size for elements) is both memory and time intensive and does not provide a better accuracy compared to the custom mesh models later used. *Auto-mesh slice* is the only one where all quality measures satisfy the minimum threshold and even the average quality is one of the best among the presented for all the measures. For these reasons this mesh has been considered as the best possible mesh (under the defined simmetry condition) for a stationary analysis and the term of comparison for an initial mesh convergence valutation. *Mesh 1* is the best affordable mesh using the sweep option and only minimal volume vs circumradius and volume vs length under the guard level. It has also the best skewness and maximum angle among all of the average values, as well as a good conditioning number. This mesh, on the other hand, is pretty time intensive when it comes to the time dependent analysis and, because of that, it was not suitable for a parameter sweep operation. *Mesh 2* is the intermediate mesh built relaxing both tank and vessel domain element size and verifying result convergence and, at least, *Mesh 3* is the best modelling option where a good convergence is still proven by the time-dependent comparison shown below. This last mesh used clearly is one of the worst proposed mesh but shows the best tradeoff between computing time requirement and quality of results.

As before mentioned, an initial qualitative comparation between meshes was conducted from a stationary analysis point of view. This showed that the stress distribution is the same for all models but clearly maximum and minimum Von Mises stress value differ because of the size of the mesh. In fact, whenever a FEM method is used the solution accuracy is strictly dependent on the mesh size: as mesh size decreases, ideally leading to a model of infinite mesh elements with a size of zero, the model moves toward the exact solution for the solved equations.

Still, considering the analysis goal of the simulation and the computational resources given, an “error” between the exact and approximate solution was obtained assuming *Auto-mesh* and *Auto-mesh slice* as the meshes closest to the real value. The other custom meshes were then compared with the average value between these two in notable points, such as the upper and lower shoulder, where maximum and minimum values of the stress distribution are located. Results show that all of the analyzed meshes show a good agreement in these points, with a maximum stress value of $34.5 \pm 7.5\ N/mm^2$ and a minimum one of $6.55 * 10^{-3} \pm 5.35 * 10^{-2}\ N/mm^2$.

Chapter 5

5 Three-dimensional model results

5.1 Stationary

Since the *Auto-mesh slice* model was the one with the finest mesh we could afford with the computer setting, this is the one used to show the vessel behaviour. As already explained in the previous chapter meshes show a good agreement in the stationary analysis, both on general stress distribution and on specific values for notable points of the geometry. Model results are presented below.

5.1.1 Von Mises stress

As already stated, Von Mises stress distribution is highly dependent on the constraint configuration and the imposed fixed constraint condition on the upper shoulder of the vessel might be an too binding hypothesis in relation to what will then be real constraints supporting the structure during its operational phase. Constraints are actually one of those aspects that should carefully be studied because their configuration could improve both the stress distribution due to the “stationary set” and the displacement configuration that will later be presented.

Moreover, this model does not contain a thermal module thus thermal stresses, largely concentrated on the divertors zone, are not considered.

For these reasons, stresses might be considerable on the area where the constraint is placed as well as on the neighbouring ones. A model upgrade that also contains thermal stresses should plan further studies on constraints settings.

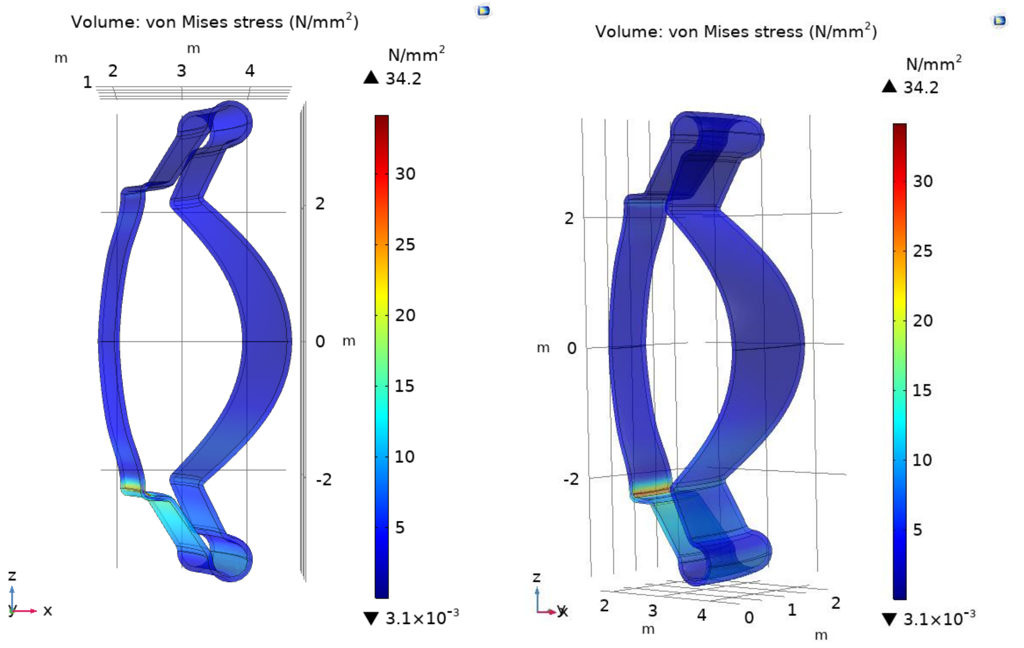

Fig. 22 - Von Mises stress distribution for the vessel

As Fig.22 shows, the mechanical stress due to constraint and hydrostatic pressure is mainly concentrated on the lower shoulder and long legged divertor of the vessel.

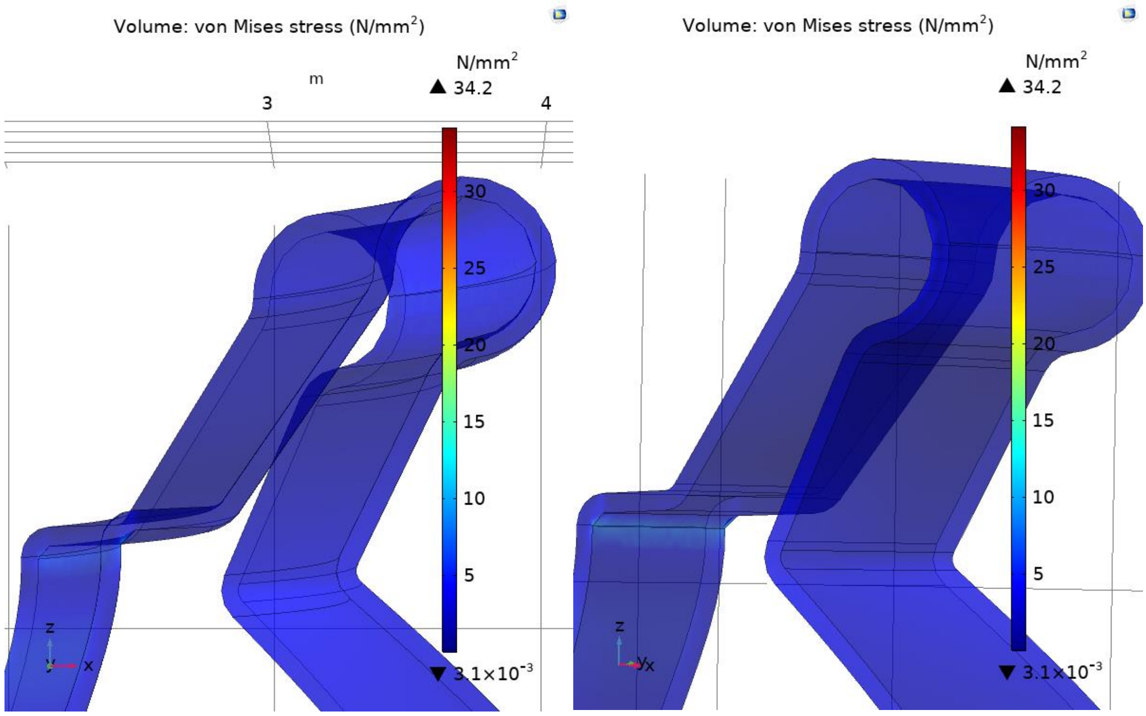

Fig. 23 - Stress distribution, detail of the upper divertor section

On the upper part of the structure the stress is neglegible, except for an edge inside the vessel (Fig. 23). This is the closest edge to the radial axis of the shoulder under constraint, and is probably caused by the own vessel structure

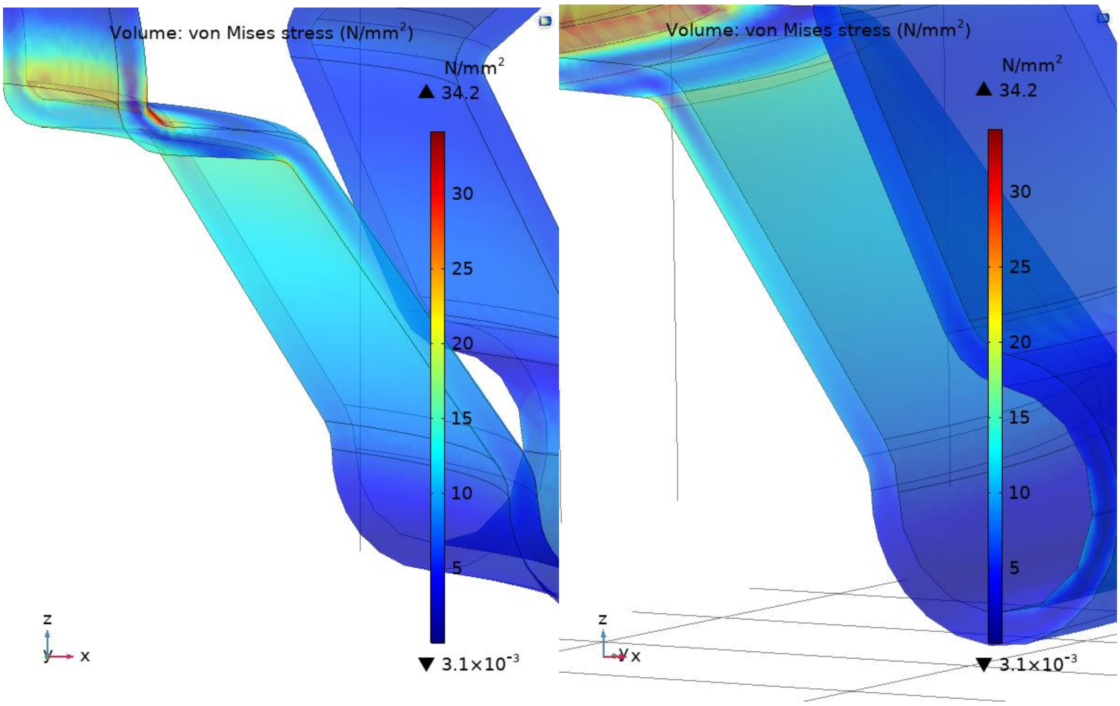

Fig. 24 - Stress distribution, detail of the lower divertor section

The lower divertor section is, on the other hand, the area where the stress is mostly concentrated on, and is caused by the hydrostatic pressure that forces the vessel to open wide along its radial direction (Fig. 24).

5.1.2 Structure displacement and absolute pressure

The displacement distribution of the structure is certainly compatible with the just presented stress distribution (Fig. 25-26).

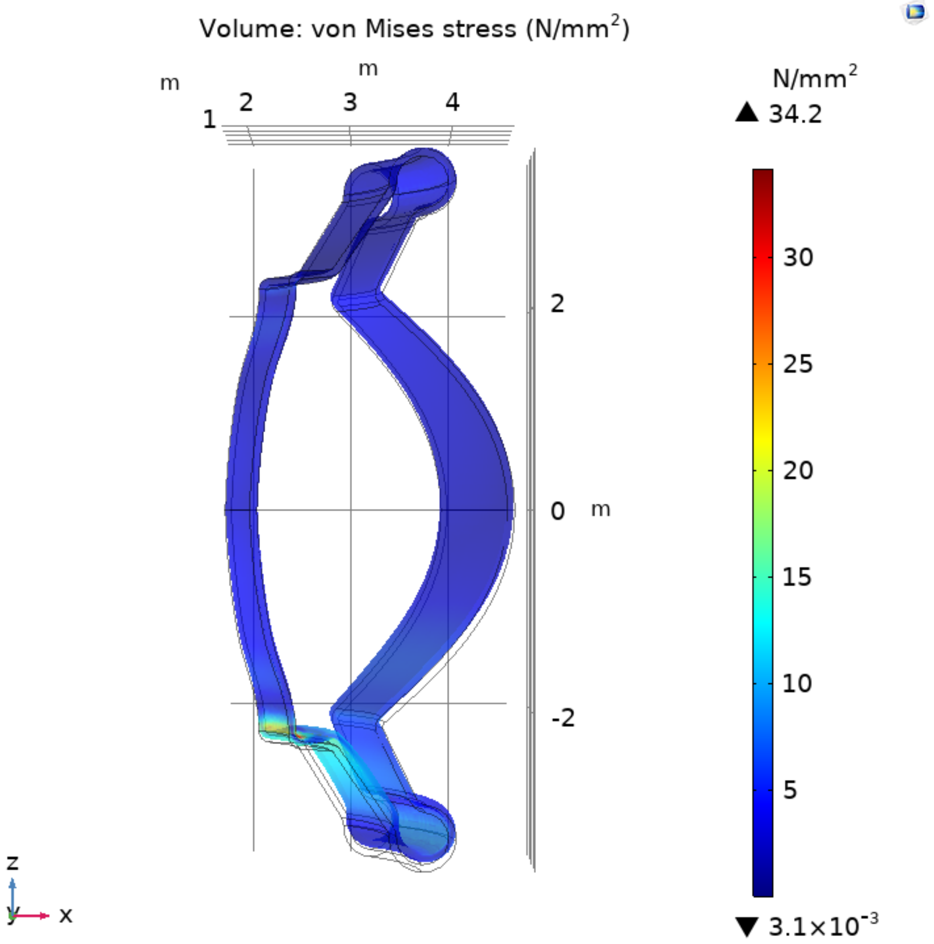

Fig. 25 - Plot of stress and visual displacement of the structure (the displacement has been visually scaled for a x300 factor)

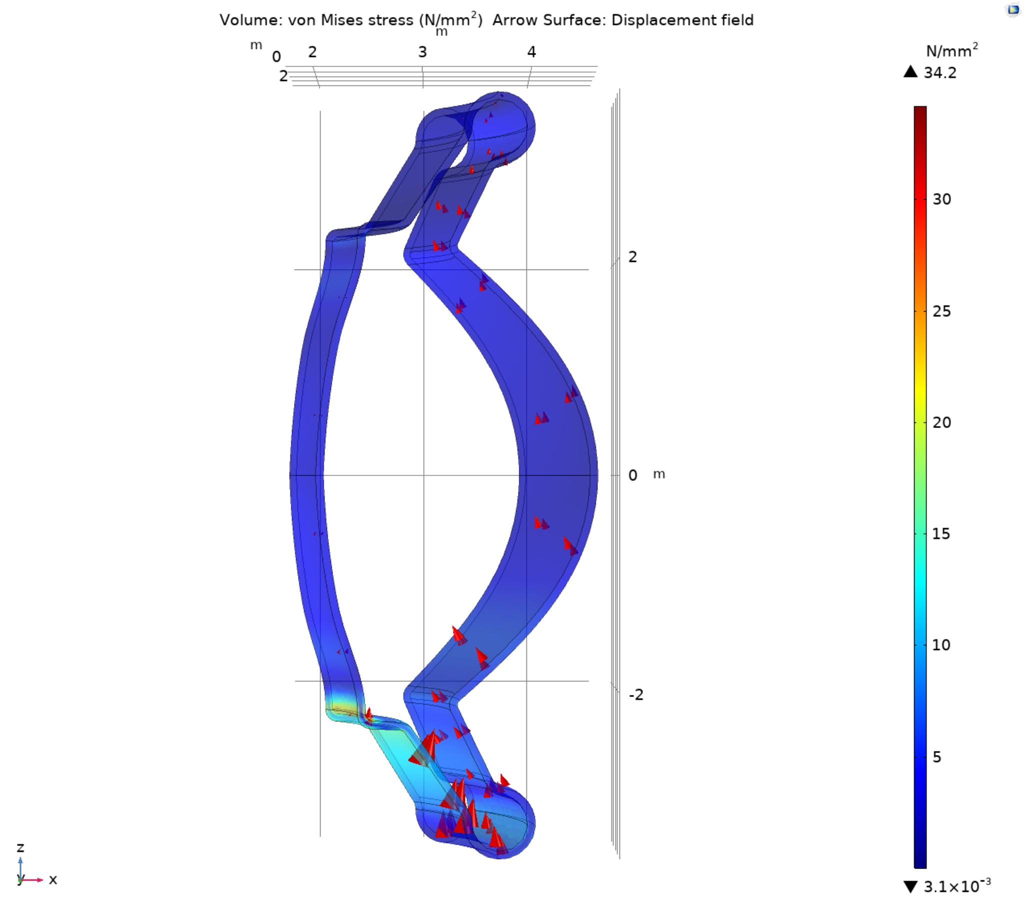

Fig. 26 - Displacement vectors of the vessel

As Fig.27a shows, the highest displacement distribution of the vessel is concentrated on the lower side of the structure (compatible with the lift stresses imposed on the vessel) and on the external part of the vessel, also defined as "belly".

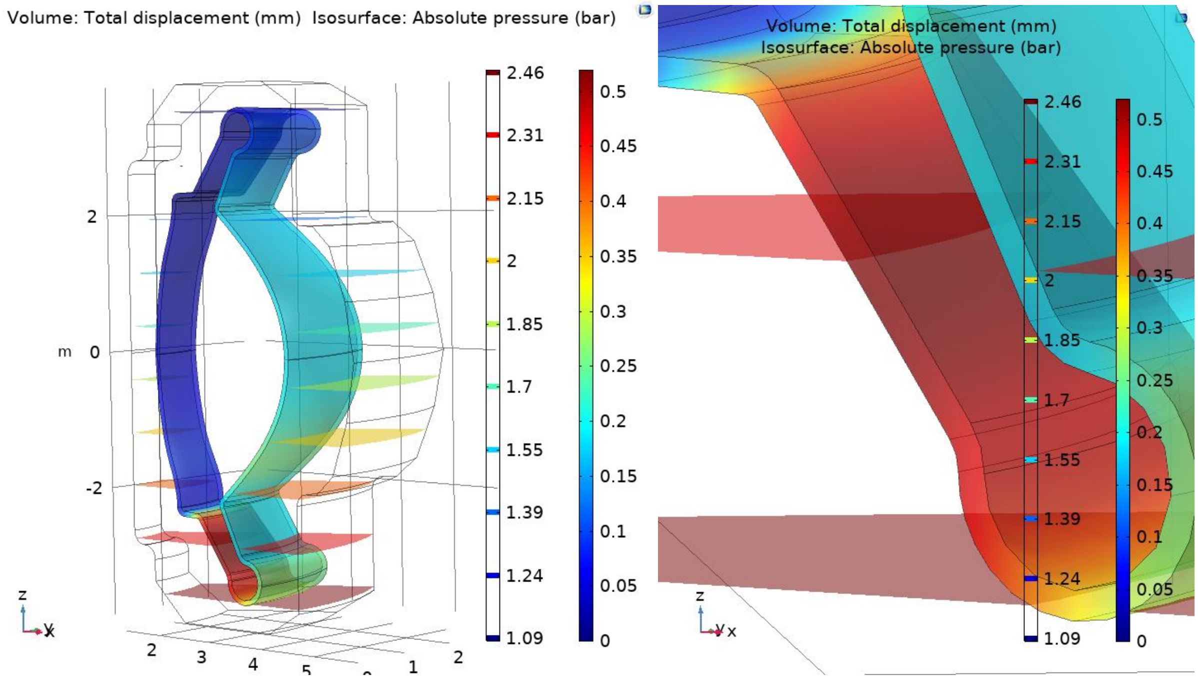

Fig. 27 - (a) Displacement plot of the structure; (b) Displacement distribution, detail of the lower divertor section

In addition, Fig.27b shows that the lower divertor leg displacement, with a peak value around 0.5 mm, might be unreasonable for the correct operativity of the vessel since this is being already one of sections under the highest thermal stress. Actually, it is worthwhile to underline that the total displacement of this region due to both the thermal and the mechanic stress could lead in harmful thermal peaks on the structure caused by the excessive proximity of the vessel with the exhausting plasma.

5.1 Mesh convergence

The time-dependent behaviour under the impulse force load could be compared only on meshes 1-3 because *Auto-mesh* presented multiple memory errors during the last phase of the simulation and the *Auto-mesh slice* is modeled with boundary symmetric options that do not swift between stationary and time dependent analysis. Forces distribution is not radially symmetric indeed and so neither can be the stress distribution. As already mentioned the disruption is simulated as a Gaussian pulse, applied on the inside of the vessel “belly”, with a range of 0.14-0.26s and a peak of 400T in 0.2s. Considering the design phase of the reactor, real forces and their distribution are currently unknown, and it was decided to consider an extreme case due to a personal communication with PSFC of MIT.

Fig 28-30 shows the behavior of a representative point for the displacement of the structure, located on the outer surface of the “belly” and along the same direction of the applied impulsive force, as well as surface integral of analyzed forces, such as lift and drag. While the first was not subdivided, since it was considered not rappresentative of the vessel motion, the latter was divided in their viscous and pressure components. The analysis was conducted for each mesh considered in the validation process both on the Pressure drag signal and on the Displacement one.

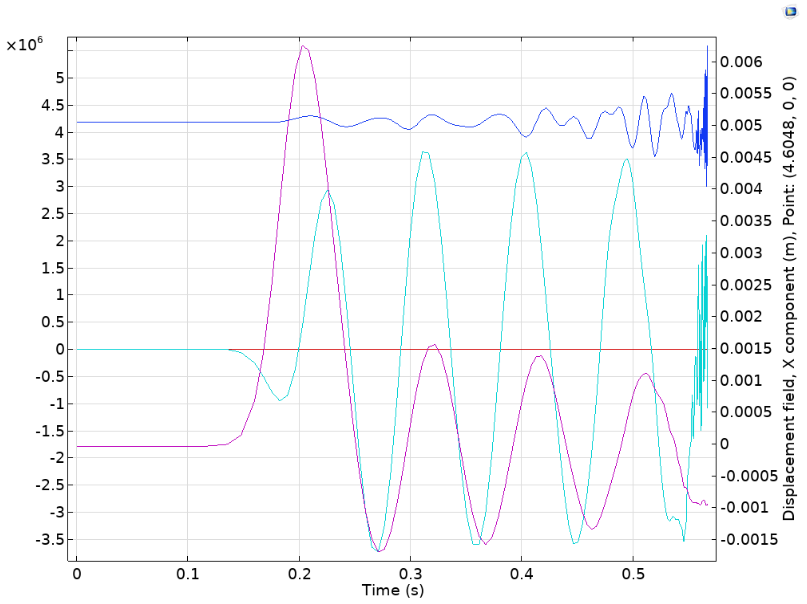

*Fig. 28 - **Mesh 1** probe displacement and exerted forces on vessel plot*

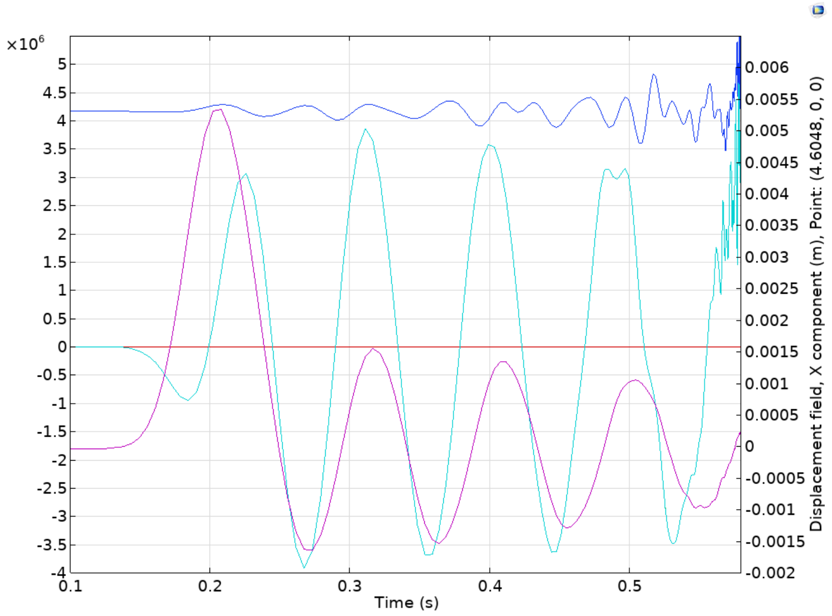

*Fig. 29 - **Mesh 2** probe displacement and exerted forces on vessel plot*

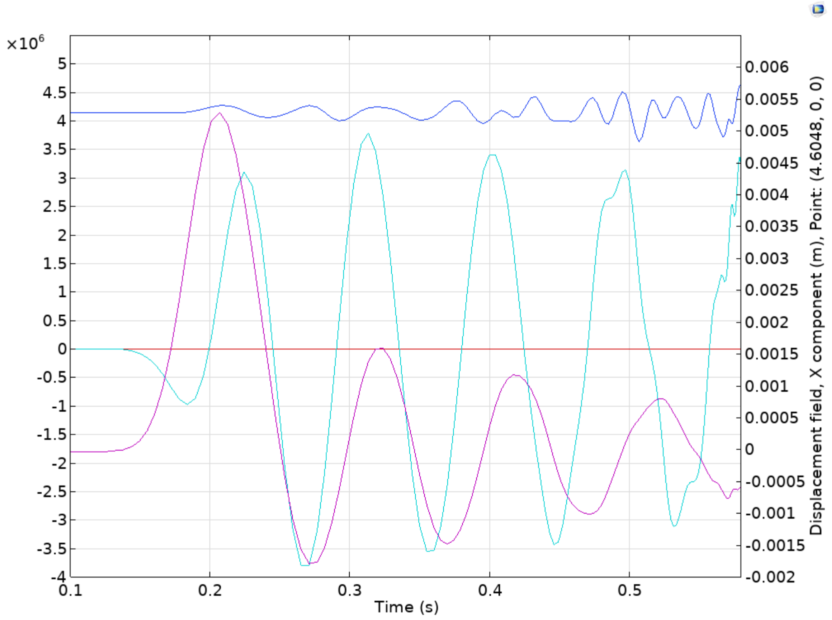

*Fig. 30 - **Mesh 3** probe displacement and exerted forces on vessel plot*

Plots presented show that for every model, under 400T of impulsive load, Lift and Drag signals over 0.54s start to reveal disturbs indicating that the behaviour of the fluid domain is probably switching from a laminar condition to a turbulent one. This is clearly shown from the bottom figure where pressure waves due to turbulence phenomena are hardly managed by the FEM model (Fig. 31b) that drammatically decreases the automatic step size (and consequently increases the reciprocal of step size) to fulfill the convergence criteria. (Fig. 31a)

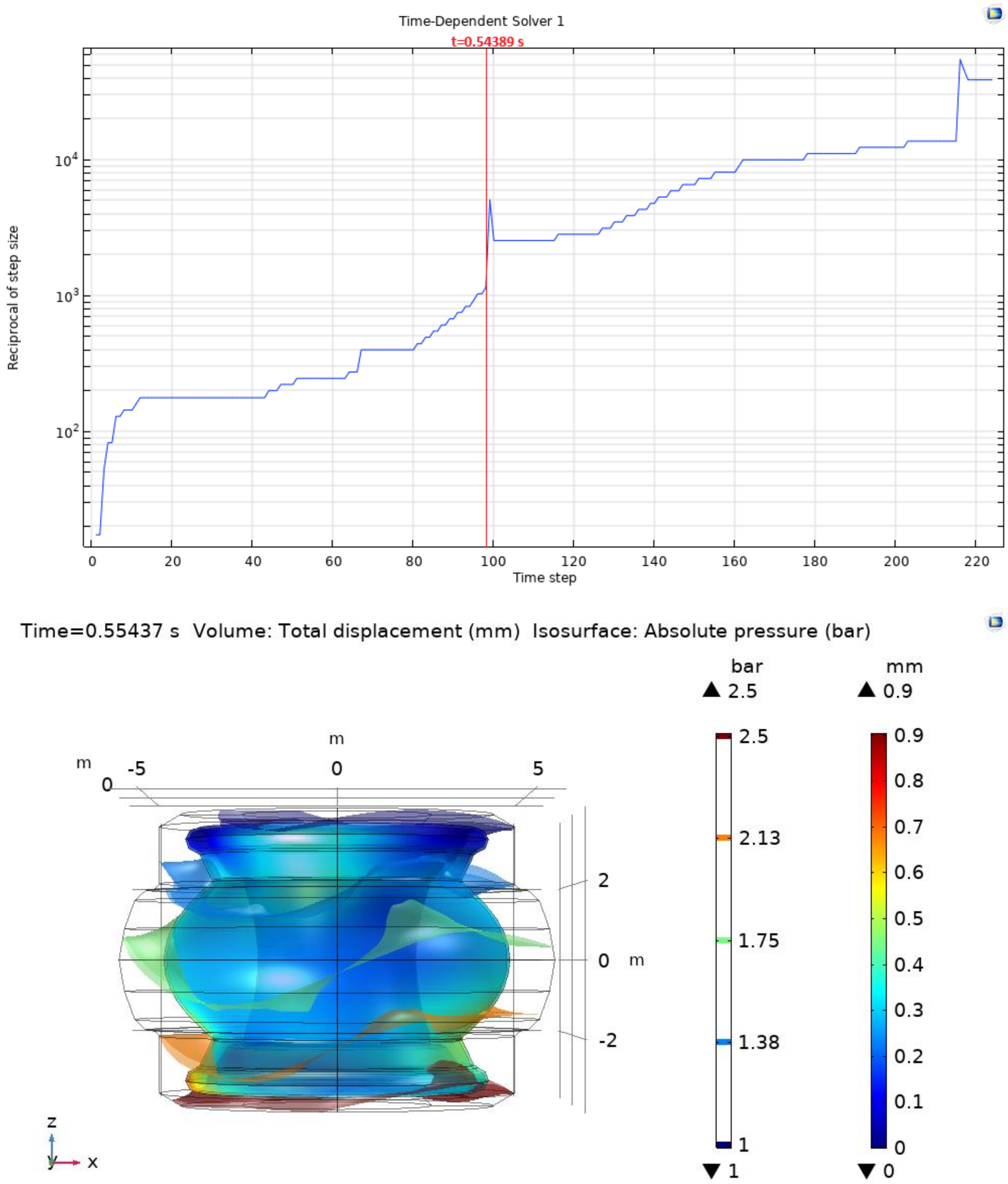

Fig. 31 - (a) Convergence plot for ***Mesh 1:*** *Reciprocal of the step size for every timestep of the analysis (b) Detail of pressure waves around 0.01s after the decrease of the step size*

For this reason the time request to complete the FEM analysis, whenever the fluid commences its turbulent behaviour, increases exponentially as the mesh size decreases and the use of a coarser mesh can greatly improve further parametrization analysis since COMSOL models do not have to be manually stopped upon reaching the turbulent phase due to the capability of the software to reach the end of the simulation in feasible times.

Such coarser mesh was decided to be the *Mesh 3* for this study because it shows convergence for an acceptable error in a qualitative kind of analysis and guarantees the achievment of the solution in terms of days.

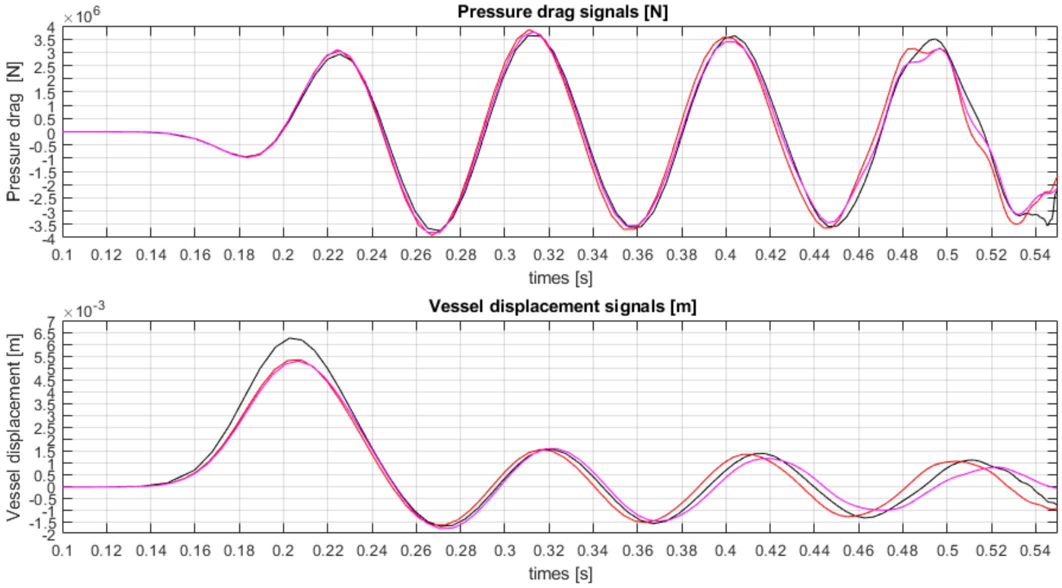

Fig. 32 - Plot of Pressure drag and Vessel displacement signals for proposed meshes in a [0.1-0.5] s time range ; (Black) ***Mesh 1****, (red)* ***Mesh 2****, (magenta)* ***Mesh 3***

Since the automatic stepping time used by COMSOL algorithm calculates signals for different time values,

a linear interpolation was performed for every mesh on the lackin time value provided by the other two meshes (Fig. 32). That way it was possible to obtain, for every time value, the statistical values useful for determining the error between meshes: the mean, the second moment and the variance. Errorbars, representative of the confidence intervals given by multiples of the standard deviation σ, were then subsequently plotted along with the mean signal in Fig. 33.

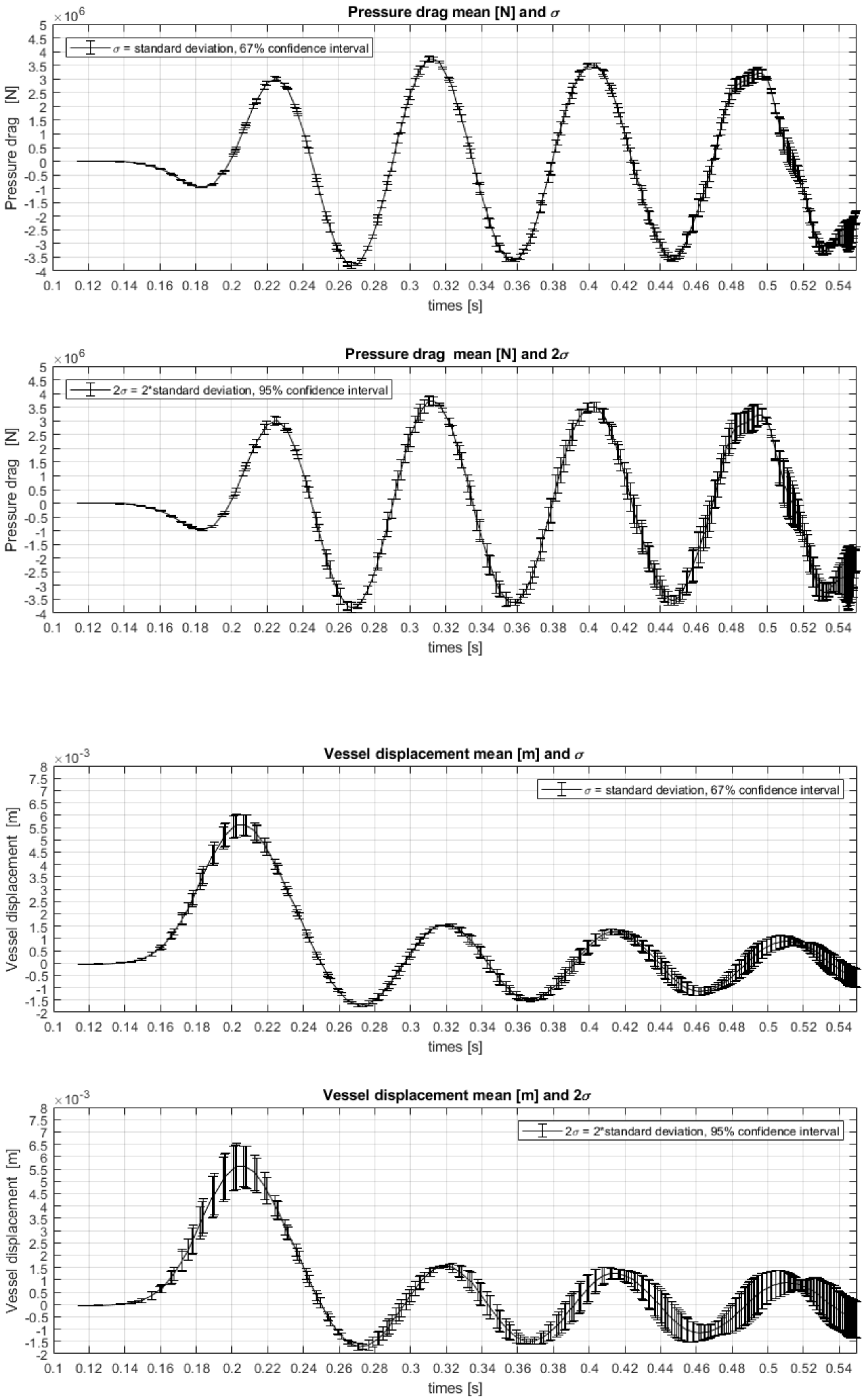

Fig. 33 - Meshes mean value and associated error

As diagrams show, convergence of meshes is verified inside an error which can be divided on the basis of belonging to a phase inside the range of *t= [0.1-0.55] s* of the simulation. The subdivision of signals into phases, which will be explained in the next chapter, is used here to show how the error varies during the simulation: it remains fairly constant in the first two phases, corresponding to a laminar behavior, but it presents a considerable increase in the last phase, corresponding to the incipient turbulent behavior.

		Phase 1 [0.14-0.26] s	*Phase 2 [0.26-0.5241] s*	*Phase 3 [0.5241-0.55] s*
Pressure drag error [N]	σ	1.5853e+05	4.4058e+05	5.8816e+05
	2σ	3.1706e+05	8.8117e+05	1.1763e+06
Vessel displacement error [m]	σ	4.7160e-04	4.0716e-04	4.2373e-04
	2σ	9.4319e-04	8.1431e-04	8.4745e-04

Table 15 - Error between meshes results

5.2 Dinamic behaviour

As previously explained, the time range for the analysis was decided to be (0.1,0.55) s. The range is wide enough to show the vessel/tank couple behaviour both in laminar and incipient turbulence phases but not enough to determine the extinction time of the vessel motion, so further studies should also integrate the analysis with an extension of the range in the turbulent phase until the equilibrium of the coupling is restored. The laminar behaviour for a 400T peak force seems to be well defined till 0.49 s (0.29 s after the peak impact value) while later dissipative mechanisms inside the turbulent flow might even stop the motion of the vessel in a shorter time compared to the one predicted with a simple laminar unrealistic model.

To show the vessel behavior, as anticipated in the previous chapter, it was decided to analize lift and drag forces on the surface of the vessel, dividing the latter into its viscous and pressure components. Obtained surface forces were then plotted along with a “displacement probe” intended as an indication of the general motion of the structure: this is located on the outer surface of the “belly”, lying on the structure’s radial symmetry plane, on the same direction of the applied impulsive force (that is the abscissa axis).

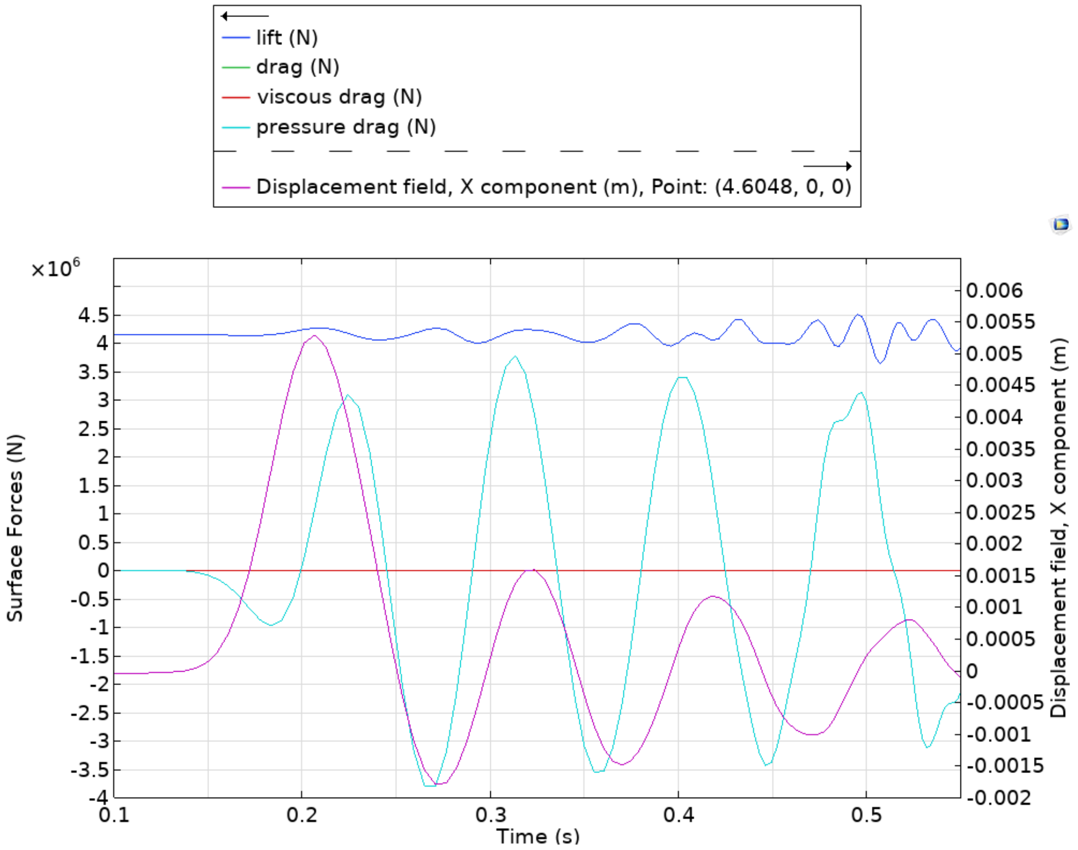

Fig. 34 - Plot of all of the force components signals along with the displacement one of the probe

Fig.34 shows that viscous drag term is negligible compared to the pressure one: this is due to the small velocity values to which the vessel is subjected, even if the FLiBe dinamic viscosity value is more than a hundred times higher than, for example, the water's one.

It is worth to be mentioned that in reality these forces are also influenced by the surface grain of the material, defined as "skin drag". However, this effect is not yet implemented in this FEM model and further studies should include an additional analysis on this topic since the viscous component may no longer be totally neglegible and it could affect the initial phase of the turbulent behaviour, if not eliminate it altogether.

As the influence of viscosity can be left out, it is admittable that the total drag force on the vessel is represented only by its pressure drag component. Therefore, on Fig.35 were plotted pressure drag and lift signals, other than the displacement signal of the vessel.

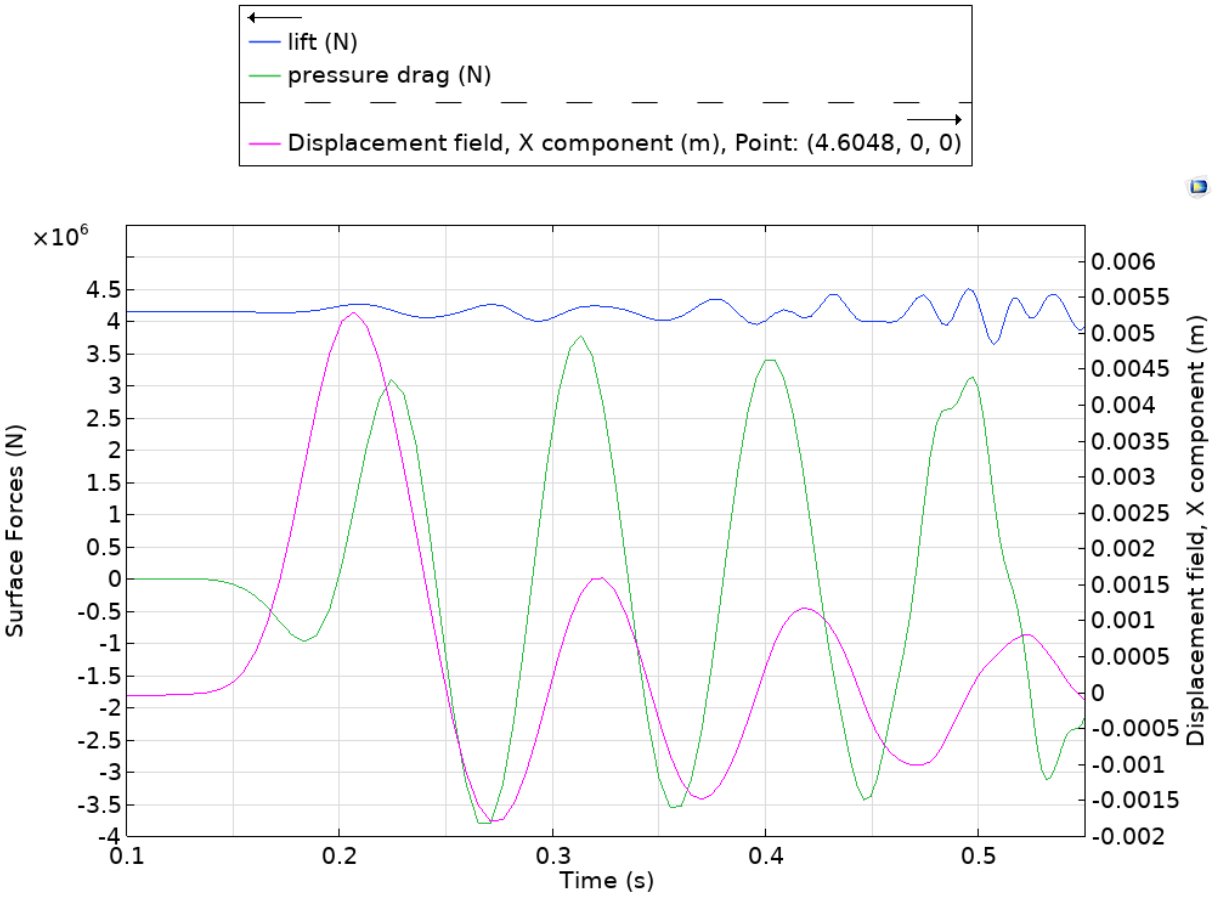

Fig. 35 - Lift, Drag and displacement signals

As the upper signals plot shows, the lift force does not have a significant impact on the vessel behaviour and remains almost constant around its initial value. Pressure drag and vessel displacement, on the contrary, show a sinusoidal trend decreasing in amplitude as time goes by, with the drag signal presenting a global maximum value in *t= 0.3099*.

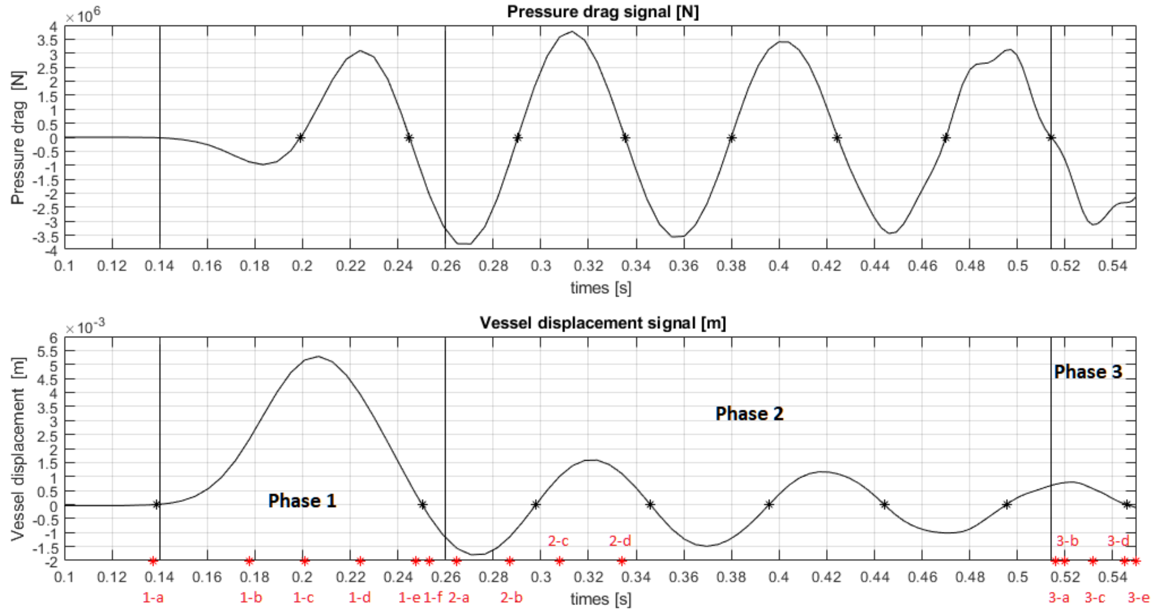

Fig. 36 - Splitting of pressure and displacement signal in phases

As anticipated in this chapter signals can be divided in phases (Fig.36) to further explain the dinamic behaviour; it is also useful to divide the geometry model in front side (x>0 region), identifiable as the region where the force is applied, and the rear side (x<0 region), identifiable as its opposite:

The first phase is defined by the time range in which the gaussian pulse is generated, and that is between *t=0.14 s* and *t=0.26 s*. In this region the vessel, after imposing an under-pressure on the front side of the fluid due to the imposed velocity, begins to move as a damped pendulum reaching his peak displacement in *t=0.2032* , with a a small positive delay compared to the gaussian pulse signal. In the meanwhile a rear side under-pressure builds up and, at the same time, the drag signals shows a negative sign meaning that the fluid is opposing resistance to the movement of the structure (Fig. 37,38 ; 1-a,1-b). Then, due to the under-pressure of the rear side, the frontal over-pressure turns into velocity and the latter changes again into rear pressure as stated from the conservation of energy; the difference between backside and frontside pressure imposes now a positive drag force that pushes further the vessel forward (Fig. 37,38 ; 1-c). After the maximum global displacement is reached the vessel begins its way back to the rest point while fluid velocity is still moving mass on the rear side of the tank building up pressure (Fig. 37 1-d); that trend does not invert until there is enough difference between frontal and back pressure and, once this happens, the fluids moves back to the front side redestributing to the sides of the vessel as a high-pressure wave towards the front side under-pressure (Fig. 37,38 ; 1-d,1-e,1-f).

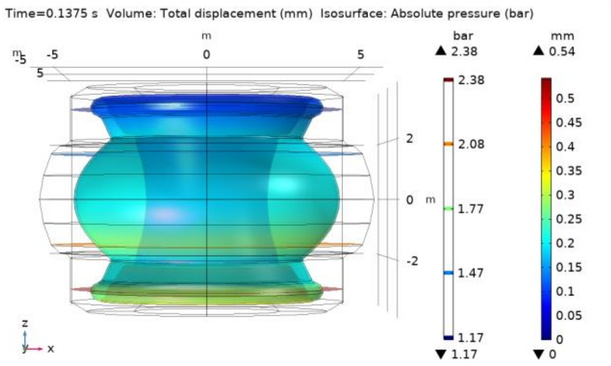

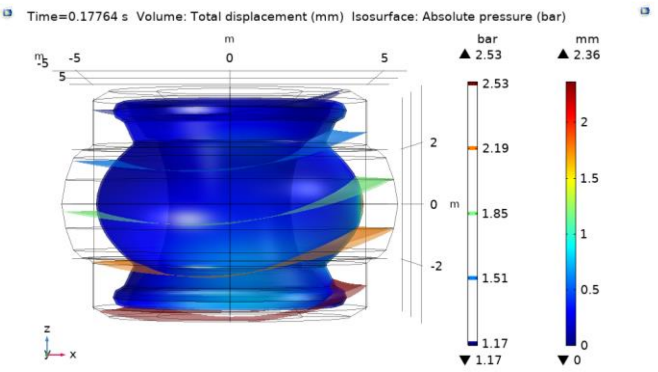

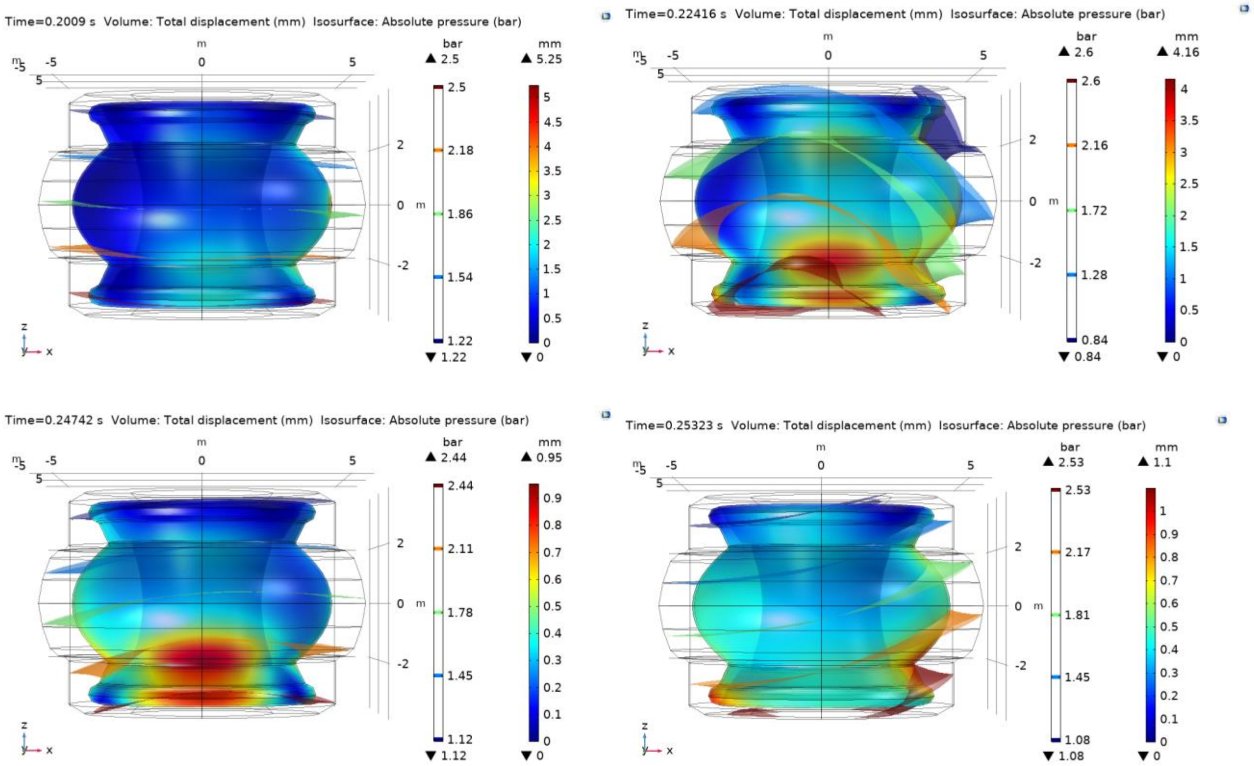
Time=0.2009 s Volume: Total displacement (mm) Isosurface: Absolute pressure (bar)

Time=0.22416 s Volume: Total displacement (mm) Isosurface: Absolute pressure (bar)

Time=0.24742 s Volume: Total displacement (mm) Isosurface: Absolute pressure (bar)

Time=0.25323 s Volume: Total displacement (mm) Isosurface: Absolute pressure (bar)

Fig. 37 - (1-a) t=0.1375; (1-b) t=0.1764; (1-c) t=0.2009; (1-d) t=0.2242; (1-e) t=0.2474; (1-f) t=0.2532

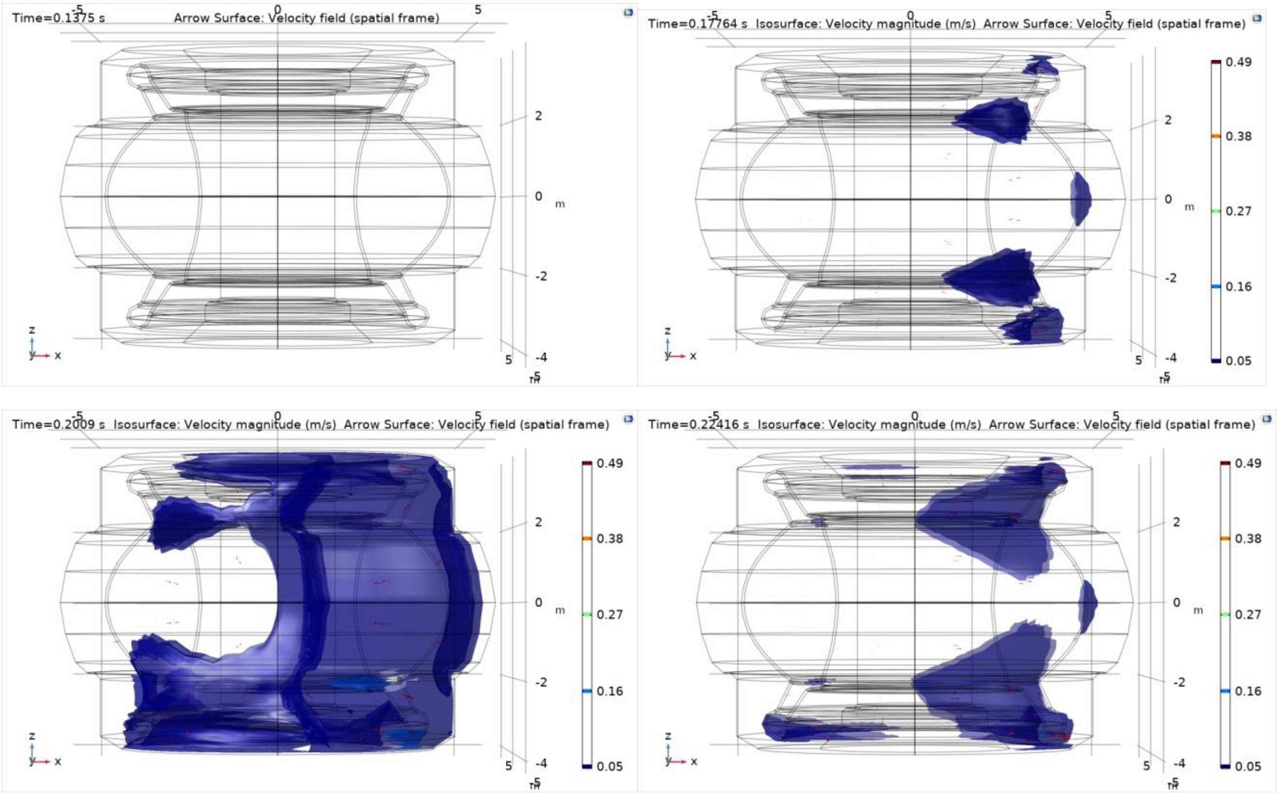
Time=0.1375 s Arrow Surface: Velocity field (spatial frame)

Time=0.17764 s Isosurface: Velocity magnitude (m/s) Arrow Surface: Velocity field (spatial frame)

Time=0.2009 s Isosurface: Velocity magnitude (m/s) Arrow Surface: Velocity field (spatial frame)

Time=0.22416 s Isosurface: Velocity magnitude (m/s) Arrow Surface: Velocity field (spatial frame)

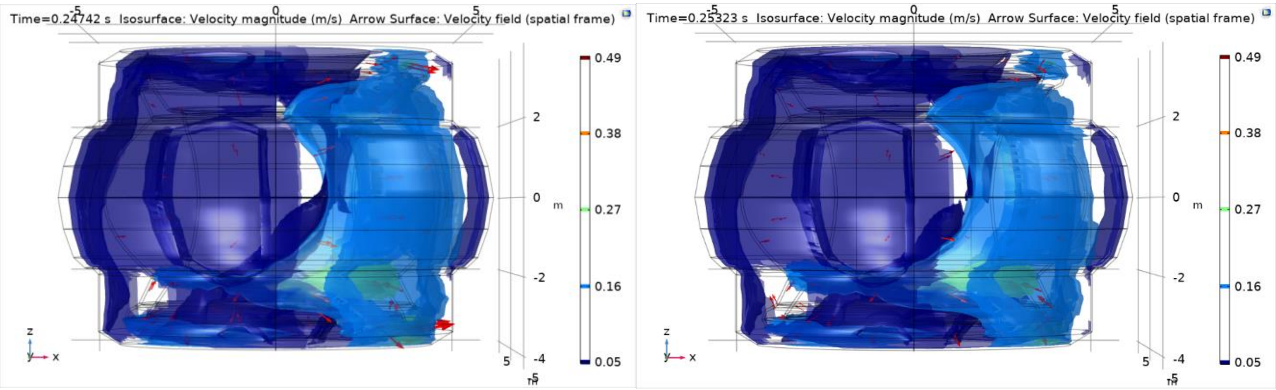

Fig. 38 - (1-a) t=0.1375; (1-b) t=0.1764; (1-c) t=0.2009; (1-d) t=0.2242; (1-e) t=0.2474; (1-f) t=0.2532

The second phase is the one represeting the laminar trend. After the signals peak (Fig. 39,40 ; 2-a), characterized by a local minimum of drag (*t=0.2649*) and displacement (*t=0.2701*) almost at the same time, the drag signal follows the displacement one's with a negative delay and reaches his global maximum value in *t=0.3099*. The almost coincident local minimum leads to the amplitude of the global maximum peak, clearly higher than the amplitude of the peak in *Phase 1*: an explanation can be that, when the vessel begins his path towards the front side, its over-pressure immediately stops building up and decreases in favor of the rear under-pressure with no additional delay, compared to other minimum peaks which would further decrease its amplitude (Fig. 39,40 ; 2-a,2-b). Moreover, the sign of the delay means that, from now on, the cause/effect relationship between fluid-structure interaction sees the pressure wave as the cause and the vessel displacement as the effect, and not viceversa as in *Phase 1*. A note concerning this time range is that the increment of the rear pressure is caused by low-pressure and high-velocity waves that moves towards it along the side regions (Fig. 39,40 ; 2-b); contrary to the high-pressure and low-velocity waves seen on the *Phase 1* that lead to an increment of the front side pressure (Fig. 39,40 ; 2-c,2-d). Later on, the different direction of vessel displacement compared to the pressure drag one's as the delay increases - other than the bland viscous phenomena - leads to the downward trend that can be noticed in the signals amplitude (Fig. 36). The pressure drag signal, in the meanwhile, follows the sinusoidal trend of the displacement with his own frequency and the cycle just explained repeats itself until the third phase.

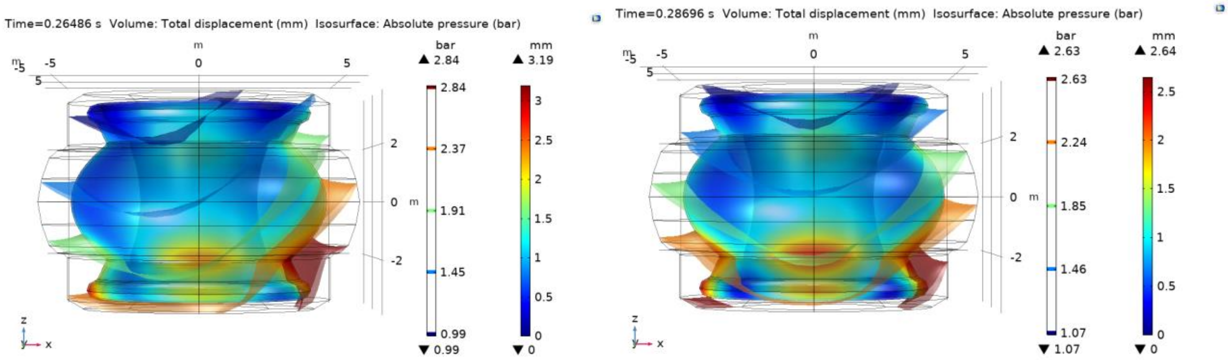

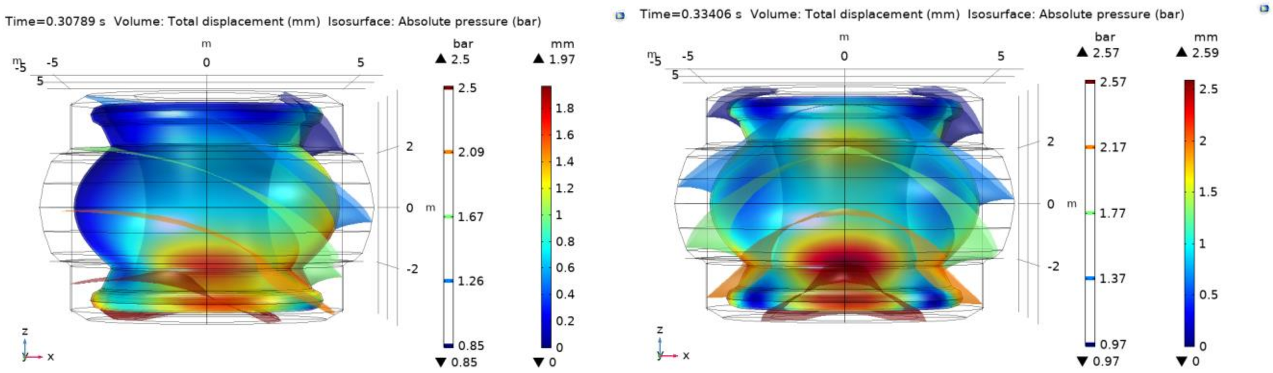

Fig. 39 - (2-a) t=0.2649; (2-b) t=0.2870; (2-c) t=0.3079; (2-d) t=0.3341

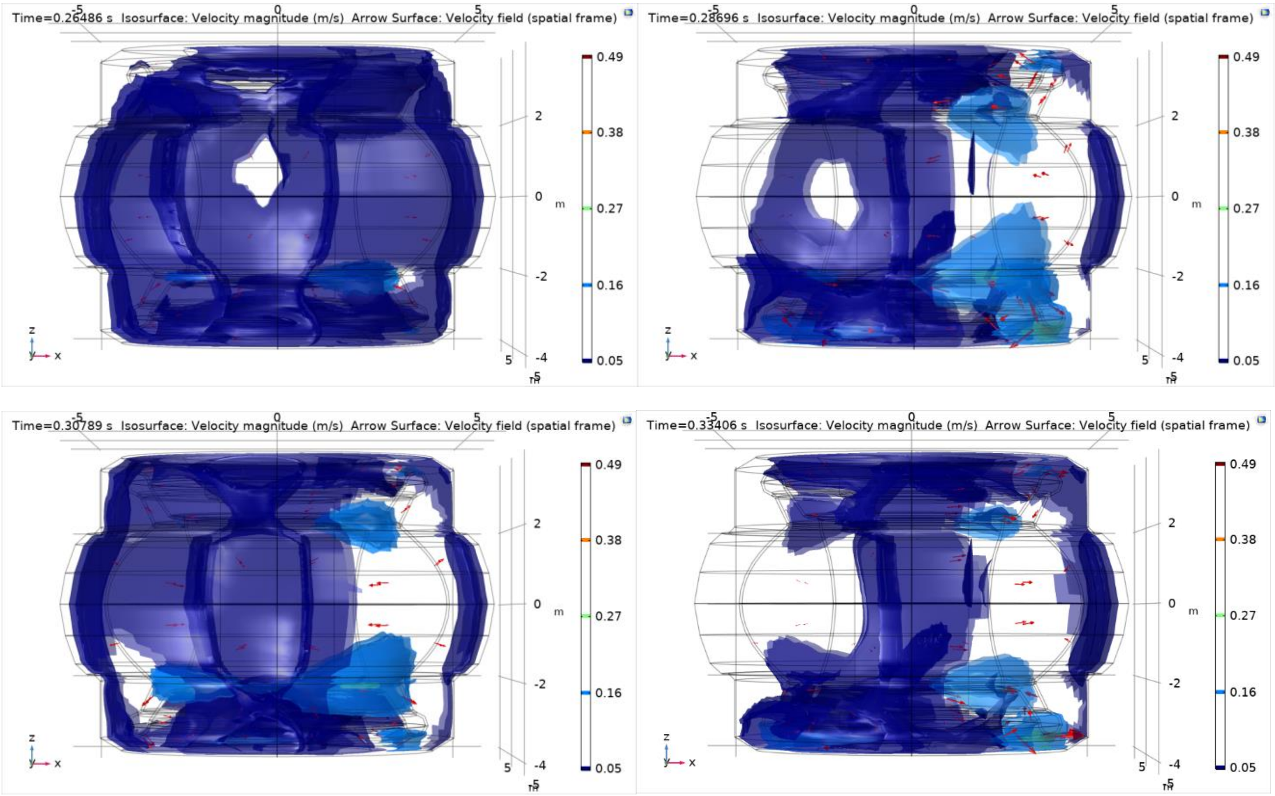

Fig. 40 - (2-a) t=0.2649; (2-b) t=0.2870; (2-c) t=0.3079; (2-d) t=0.3341

The third and last phase is the incipient turbulence phase and an hypotesis on how it forms will be presented later; after this phase the disturbance in the signals becomes too sustained for the analysis to be considered reliable.

These phases, as shown in Fig. 36 and later in Fig. 44, are defined through the use of significant points (zeros, maxs, mins) of signals and their relative derivates: all of these informations were obtained through a simple script in the MATLAB computing environment. Therefore, once zeroes were determined it was also possible to calculate frequencies of signals half-periods: *f1* for the pressure drag and *f2* for the vessel displacement (Tab. 16).

f1 [Hz]	10,935	10,989	11,124	11,194	11,215	10,999	11,316
f2 [Hz]	4,483	10,454	10,439	10,019	10,367	9,735	9.927

Table 16 - Frequencies for semiperiods of pressure drag and vessel displacement signals

The first frequency vector shows a trend that seems to remain almost constant around the arithmetic average frequency value of *f=11,110 Hz*. The other vector, on the contrary, shows immediatly a decreasing trend, except for two values, the first and the last one's: the first value should not be considered because it derives directly from the frequency of the Gaussian load, in this case *f=4.16 Hz*; the last value is calculated over the transition between laminar and turbulent behaviour and it is not representative of the second phase tendency. The observation of a downward trend on the displacement signal leads to the hypotesis that the difference between signal frequencies is directly connected to the emergence of turbulent conditions: these begin around the local zero of the pressure drag signal in *t=0.5142* (Fig. 41,42 ; 3-a,3-b) and consolidate themselves through all of the *Phase 3*. When the vessel moves towards a direction, represented by the sign of the velocity, and the pressure drag signal is characterized by a different sign and a high derivate in the same range, the under-pressure region shows such low values on the pressure field that gradients induce turbulent phenomena as the velocity increases and locally surpasses the laminar behaviour limit (Fig. 41,42 ; 3-c,3-d). This turbulent behaviour starts showing itself as side vessel waves with a lower amplitude (Fig. 41,42 ; 3-e) and an higher frequency, compared to the main wave signal: it present itself in like manner as a noise signal would, increasing until the "main wave" is hardly distinguishable as a variation of the average value of the high frequency disturbance.

Whenever this happen the *Phase 3* can be considered over, and the presence of a fully turbulent fluid behavior can be represented in Fig. 43.

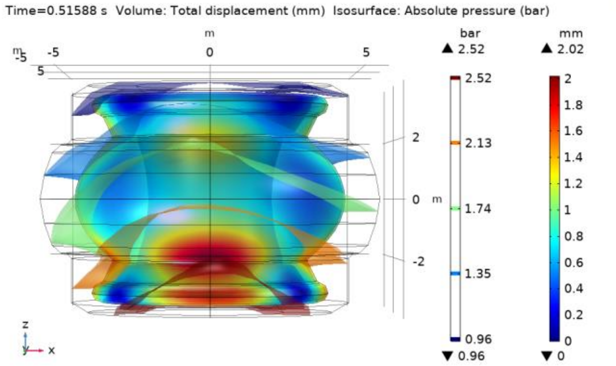

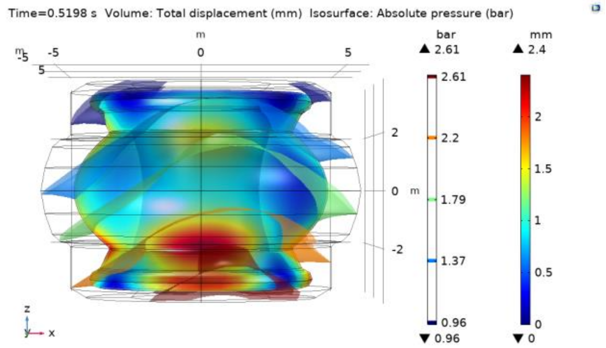

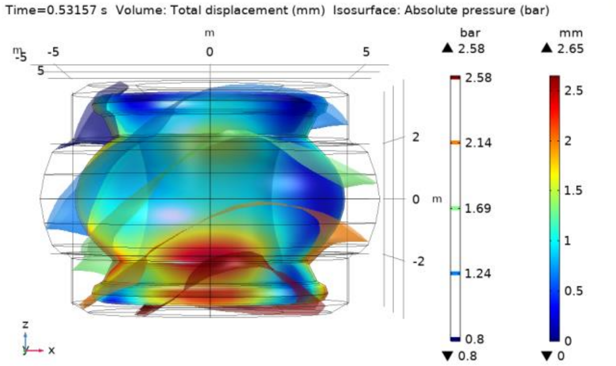

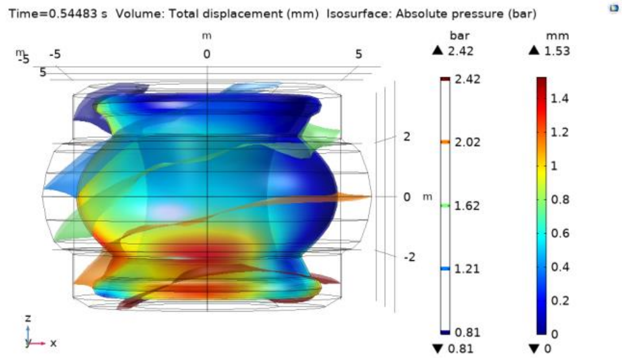

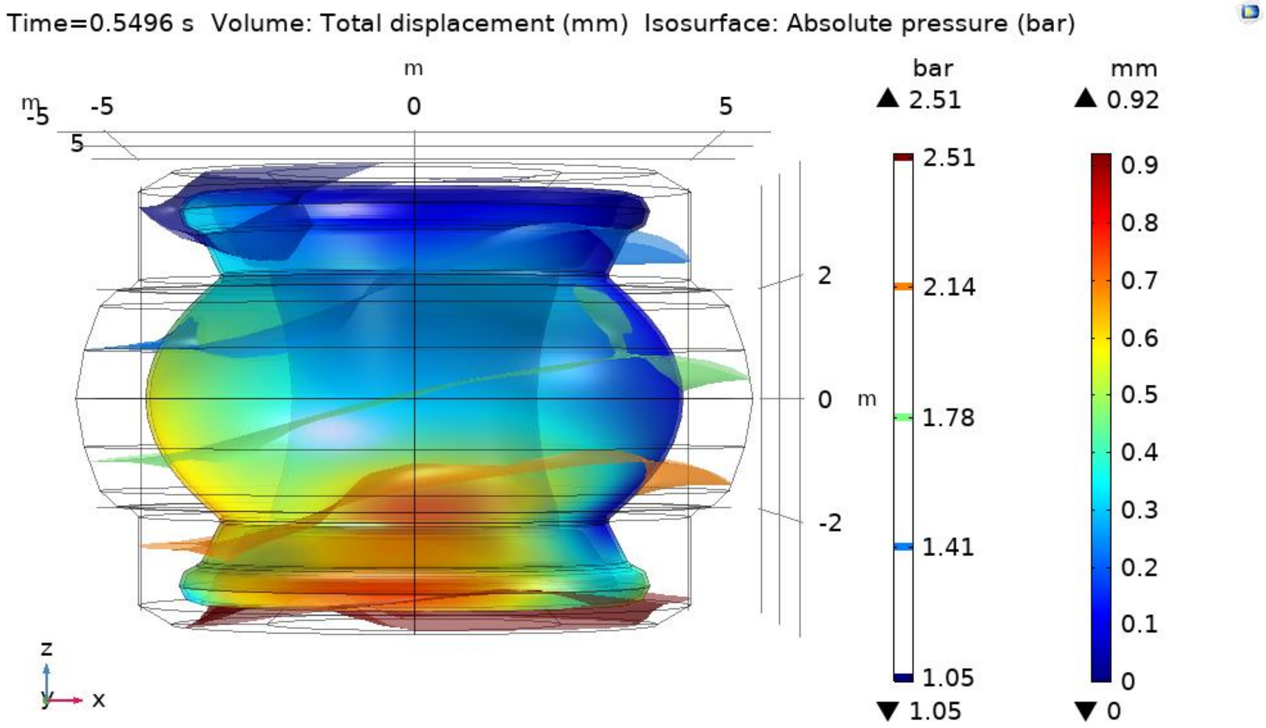

Fig. 41 - (3-a) t=0.5159; (3-b) t=0.5198; (3-c) t=0.5316; (3-d) t=0.5448; (3-e) t=0.5496

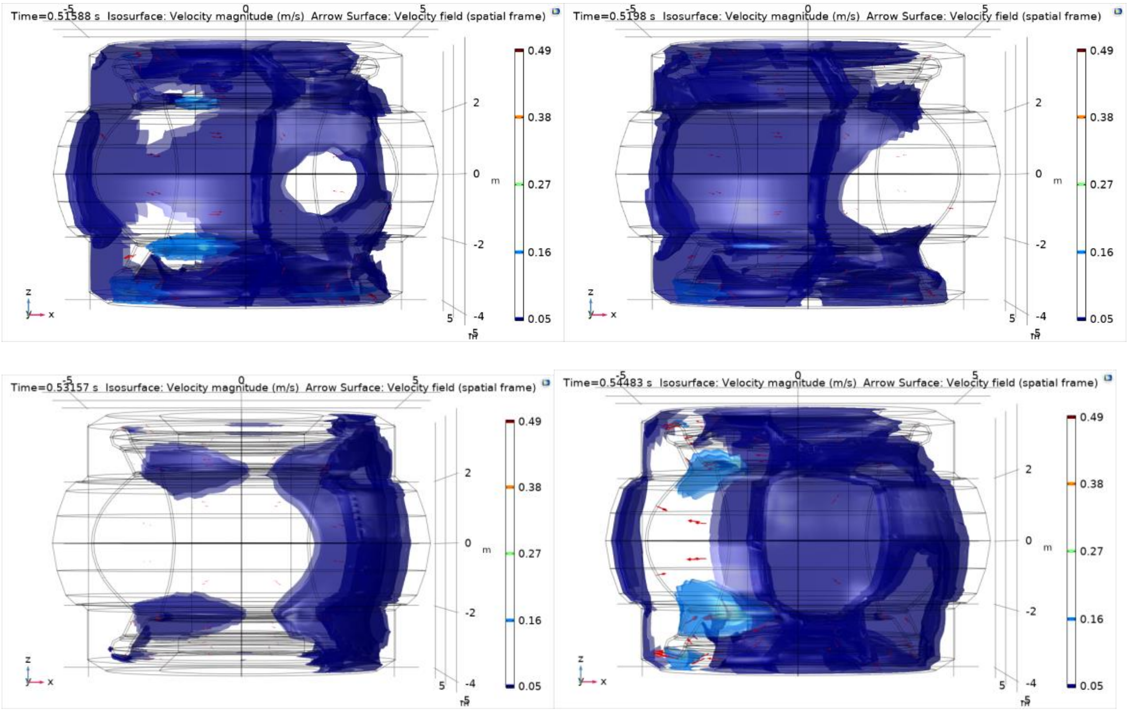

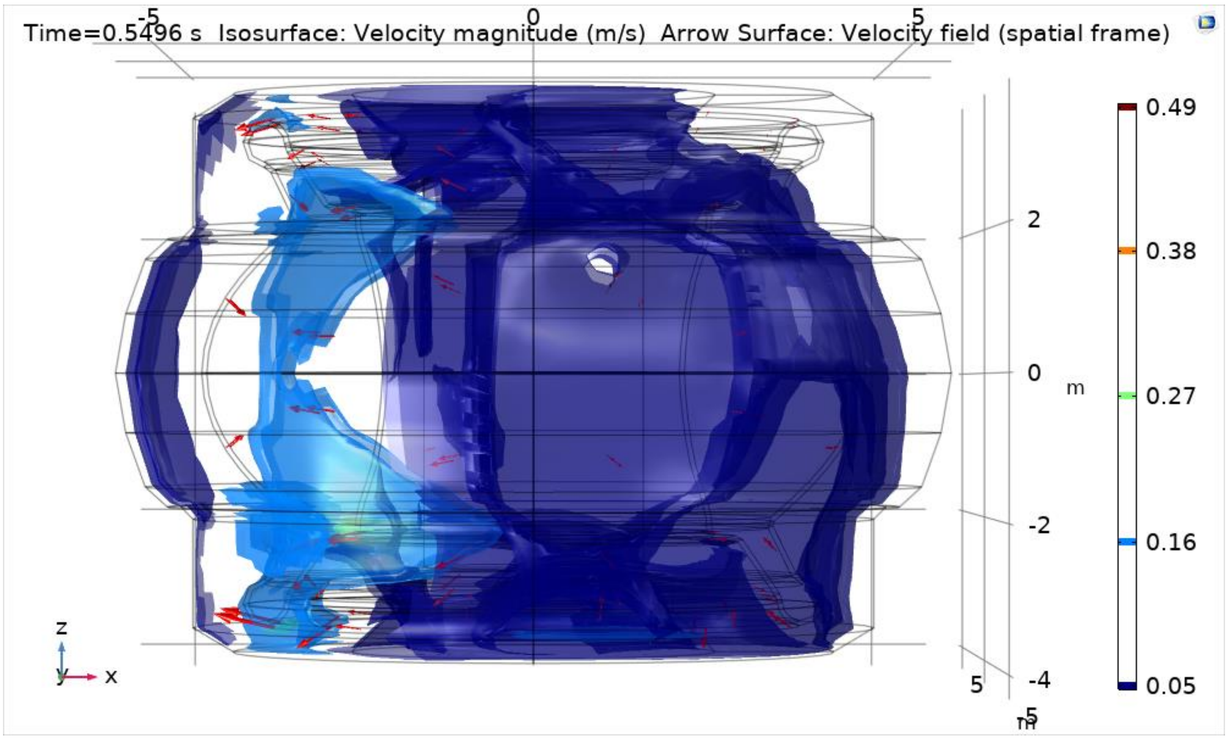

Fig. 42 - (3-a) t=0.5159; (3-b) t=0.5198; (3-c) t=0.5316; (3-d) t=0.5448; (3-e) t=0.5496

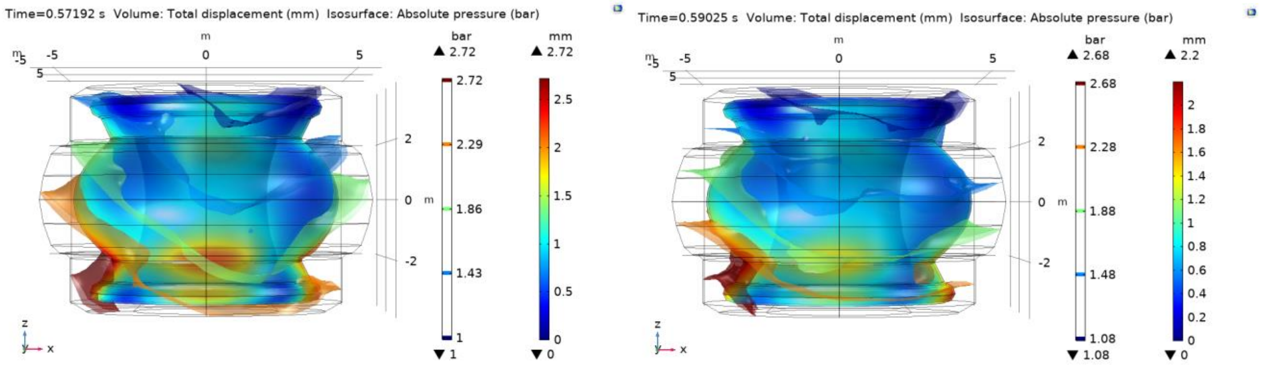

Fig. 43 - Plot of fully tubulent behaviour (a) t=0.5720; (b) t=0.5925

To explain the above hypotesis the pressure vector and the vessel displacement vector were derived: the drag derivate returns the information about the degree of increase of surface forces as well as the abscissa of local maximums and minimums; the second derivate, in addition to these, also returns the information about the displacement scalar value's versor or, in other words, the "direction" toward which the vessel displacement is moving (Fig. 44).

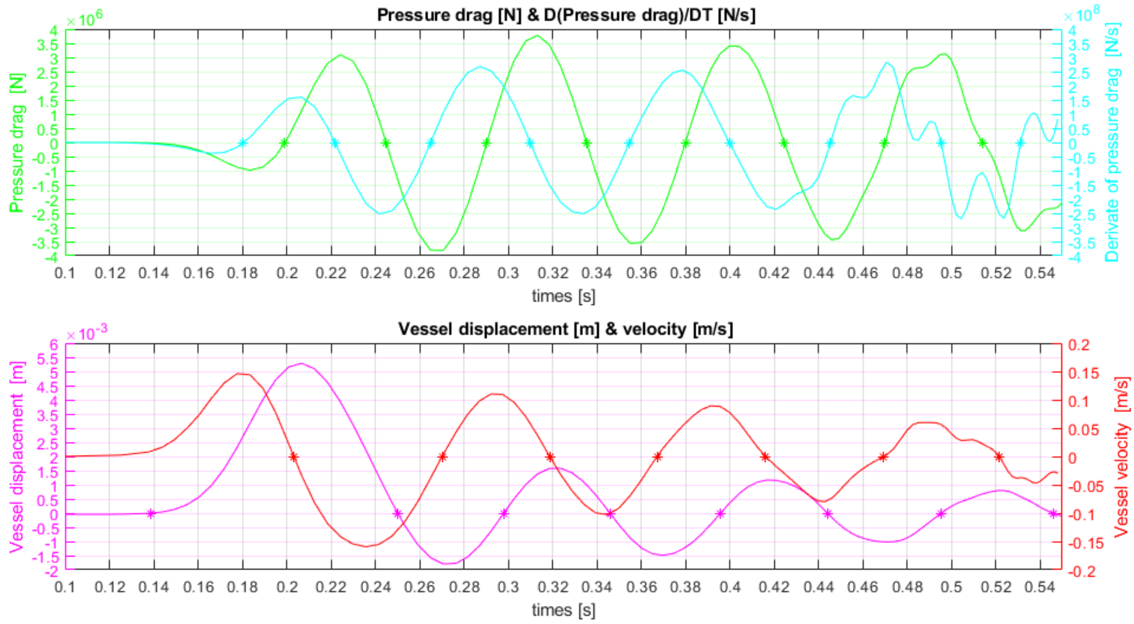

Fig. 44 - Plot of signals and relative derivates

As Fig. 45 shows, the begin of a turbulent behaviour can be found around the above mentioned *t=0.5142* : from now on, for a short period of time, a great part of the pressure wave has a negative sign, whereas the vessel velocity signal, representing the direction towards which the vessel is moving, still remains positive. At the same time, the pressure drag derivate (Fig .44) shows a sinusoidal “peak” between two global minimum values, and that means that pressure drag gradients in this region are higher that one would expect during a viscous dissipation. The reason of this behaviour could be related to the fact that, from the immediately preceding half-period of the velocity and pressure signals to the fully turbulent phase, these two signals become substantially synchronous because of the downward frequency trend of the displacement signal: that means that vessel and fluid waves are moving toward the same direction at the same time. This seems to give sustance to the above hypotesis for an example force of 400T, but it is presumable that lower forces might not present at all the same turbulent trend since pressure gradients could not be enough to generate it.

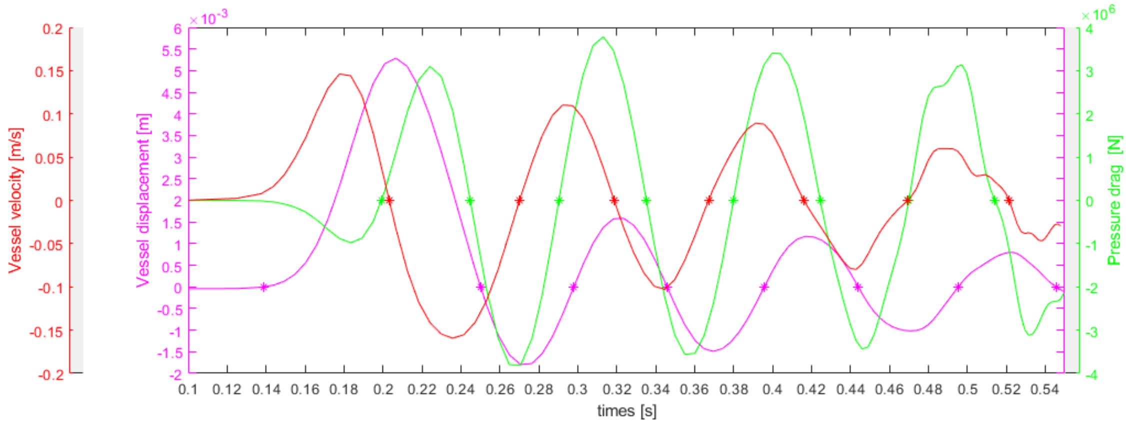

Fig. 45 - Comparative plot of pressure, vessel displacement and velocity signal

5.2.1 Preliminary force parameterization

As previously shown the model can be used to analyze the laminar trend and it is not suitable for the turbulent one. But it could also be assumed, as the modulus of the impulsive force varies, that turbulent behaviour occurs or not: if the modulus is low, the turbulent trend may not occur at all since the pressure gradients inside the blanket are not sufficient for it to be generated. As the modulus rises, the incipient turbulence should always reappear under the same conditions shown above. This is valid as long as the impulsive force is so high that the pressure gradients, necessary for the onset of the turbulence, occur even without the necessary conditions of sign opposition between velocity and pressure drag signals on one side, and high pressure gradients on the other side.

It is therefore important to underline that the hypothesis of incipient turbulence in the case of simultaneous occurence of the aforementioned is a necessary condition, but not a sufficient one's: other conditions not identified in this study should arise in addition to it. This is shown by Fig. 46, where it is clear that, on the basis of a first parameterization of the intensity of the applied force, even impulses higher than the 400T analyzed, as example 600T, do not present a condition of turbulence.

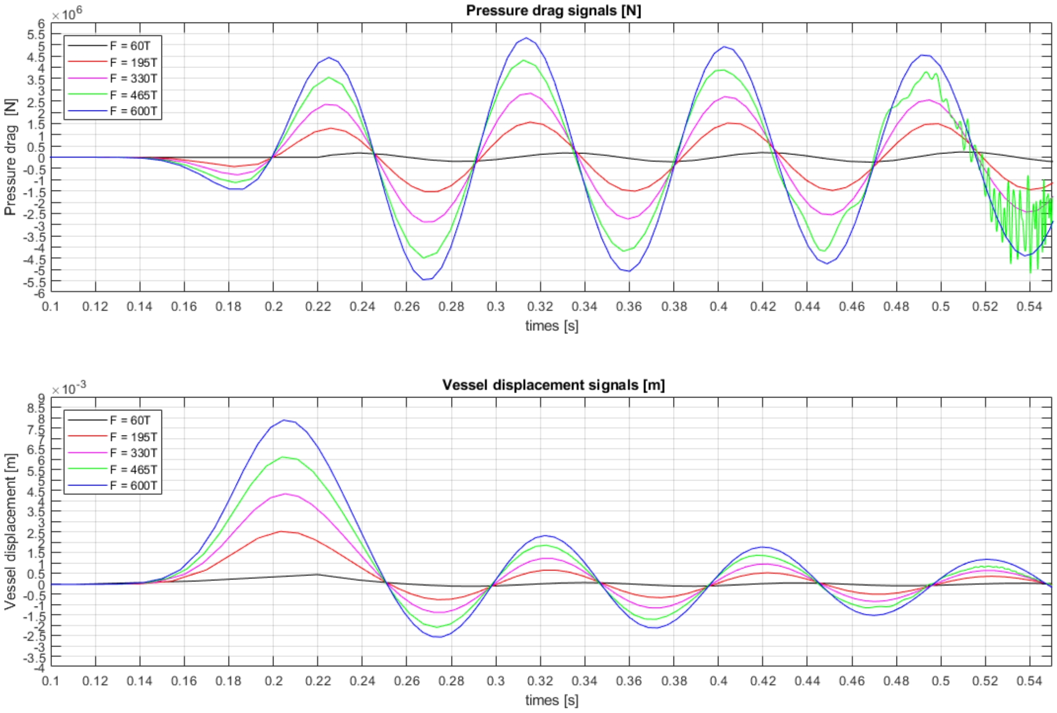

Fig. 46 - Force module parameterization

Because of that, further analysis both on the variation of the force modulus and on the position where the impulse force is applied should be conducted, also considering that a disruption is most likely to happen in the proximity of divertors, since that is the point subjected to the highest probability to see a plasma contact due to an accidental variability in the magnetic field configuration.

The above diagrams also show that the frequency appears to be indipendent from the modulus of the applied force, and may can only depend on the geometry of both the structure and the FLiBe tank and on the type of fluid inside it. In any case, a semplification in the geometry of both the elements could calrify the cause of this result.

Conclusions

Regarding the ARC reactor design field, in a thriving conceptual phase, studies simultaneously combining several physics are necessary to ensure the correct functioning of the reactor, since almost all of the physical quantities involved reside in a largely unexplored field. Particularly, during extreme unusual situations such as a disruption one, the mutual contact between the plasma and the structure leads to a series of chain events: more than a million kelvin temperature and extreme magnetic torques on the vessel layers cause a disruptive mechanical stress on the entire structure and a conspicuous transfer of residual energy from the vessel to the fluid blanket.

The "immersed pendulum" modelling technique proved effective, but it usually reduces the fluid component as a simple closed form equation representing the hydrostatic pressure exerted on the structure. That simplification is acceptable in a dynamic model as a rule, as far as the model presupposes an infinite volume of fluid around the pendulum, and therefore in this situation CFD models are often computationally heavy and not suitable for the job. On the other hand, analysis on the behaviour of this body within a closed and limited environment, such as a tank, have not yet been conducted, even though the mutual interaction between fluid and structure seems to have an effect on the movement mechanics of the pendulum, represented in this case by the vessel, whenever its trend changes from laminar to turbulent. This study wants to show that, particularly in case of a disruption, an analysis of the fluid behaviour might be usefull to prove and further enhance the reactor safety, as well as to slightly adapt the vessel and tank geometry in order to better control (or even exploit) the high forces involved. That said, the approach that consist in coupling structural and fluid dynamic physiscs, also known as FSI coupling algorithm, turns out to be effective to determine the vessel blanket couple behavior, both in a stationary analysis and in a dynamic one's.

The proposed static model, given the semplification of a single, uniform layer of Inconel 718, well represents the stress and displacement distribution on the vessel and could be used for an initial check phase of the peak stress values along notable points of the geometry, such as constraints linking the vessel to other components of the structure. However, the first step towards a model more consistent with the reality of the structure should be a multi-layer upgrade: in fact, both the thickness of the different materials and the type and positioning of the rigid connections between them could significantly change the stress distribution.

Furthermore, studies on the type of constraint to which the vessel is subject should be carried out, as well as the position of these "anchors". This is extremely important since their definition would modify the static stress distribution and the entire dynamic behavior.

In addition to this, the model does not comprehend the thermal behavior of the structure, and the displacement due to the dilatation of the structure should be added to the one derived from the FSI in future works. Other studies show a contribution due to the thermal effect about an order of magnitude higher [15], and the resulting tensions would not be neglegible.

The dynamic model correctly computes the mutual interaction between the structure and the fluid, but the analysis did not show an agreement as good as the static one, due to the lack of computational power that would have led more detailed models to provide a solution in extreme computation times. Anyhow, the error of the signals presented shows that all of them have clearly a similar trend between the meshes, but more precise values and a well converged solution could be obtained using a computational cluster.

The model proved suitable for determining the reciprocal interaction between pressure waves and displacement of the structure under impulsive load, but it was decided not to show the stress distribution of the vessel in the dynamic behaviour, that is indeed not fully representative of the real stress caused by a disruption. This is due to the fact that the impact has been modeled as a force exerted on a punctual surface:

this is a singular point of the model equations, and while the distribution around the point does represent the behaviour of a real impact, the maximum value of the stress, as predictable, is directly influenced by the mesh size since the pressure is calculated as the force applied on a surface. In fact, as the mesh size decreases, the punctual force is gradually distributed on a smaller surface and the maximum of the stress distribution theoretically leads to an infinite value when the surface becomes punctual.

The above mentioned opens up welcome opportunities to future developments regarding this modelling technique. One of them should concern a general simplification of the geometry both of the vessel and the FLiBe tank, reducing the large number of variables involved in the turbulence generation mechanism in order to identify in detail the triggering causes of the phenomenon.

Bibliografy

[1] «iter.org,» [Online]. Available: https://www.iter.org/newsline/-/3382.

[2] «Brookhaven national laboratory,» [Online]. Available: https://www.bnl.gov/magnets/hts-magnet-program.php.

[3] E. A. Prato e M. Zucchetti, «New Advanced Materials for Energy Production: The Arc Fusion Reactor and MHD phenomena in the FLIBE Breeder,» *International journal of ecosystems and ecology science,* vol. 9, n. 3, p. 8, 2019.

[4] H. Zerriffi, «The environmental, health, budgetary, and strategic effects of the Department of Energy's decision to produce tritium,» p. 15, Jannuary, 1996.

[5] C. N. I. Centre, «An overview of tritium production,» [Online]. Available: https://inis.iaea.org/collection/NCLCollectionStore/_Public/35/032/35032523.pdf.

[6] P. Bettini e R. Specogna, «Computation of stationary 3D halo currents in fusion devices with accuracy control,» *Journal of Computational Physics,* vol. 273, pp. 100-117, 14 May 2014.

[7] A. A. Sonin, «Equation of Motion for Viscous Fluids,» 2001 (8th edition). [Online]. Available: https://ocw.mit.edu/courses/mechanical-engineering/2-25-advanced-fluid-mechanics-fall-2013/equations-of-viscous-flow/MIT2_25F13_Equat_of_Motio.pdf.

[8] C. Andersson e D. Ahl, «Fluid Structure Interaction Evaluation of two coupling techniques,» *Technical report, IDE1135,* June 2011.

[9] «Wikipedia,» [Online]. Available: https://en.wikipedia.org/wiki/COMSOL_Multiphysics.

[10] R. Serrano-López, J. Fradera e S. Cuesta-López, «Molten salts database for energy applications,» *ScienceDirect,* vol. 73, pp. 87-102, November 2013.

[11] «Comsol Multyphysics-Physics-Controlled Mesh settings,» [Online]. Available: https://www.comsol.it/support/knowledgebase/1261.

[12] «COMSOL Blog-How to Inspect Your Mesh in COMSOL Multiphysics,» 12 May 2017. [Online]. Available: https://www.comsol.it/blogs/how-to-inspect-your-mesh-in-comsol-multiphysics/.

[13] C. Multiphysics, *COMSOL Multiphysics reference manual-Meshing techniques-Mesh element quality and size.*

[14] «COMSOL Multiphysics Reference Manual-Deforming Fluid Domains,» [Online]. Available: https://doc.comsol.com/5.5/doc/com.comsol.help.comsol/comsol_ref_deformedmeshes.25.02.html#803990.

[15] S. Segantin, «Load following concept feasibility of arc reactor power plant based on thermo-mechanical analysis of the vacuum vessel,» *Master's thesis,* 2016/2017.

List of Figures

List of Tables